Transient Response in a *Z*-Level Ocean Model That Resolves Topography with Partial Cells

RONALD C. PACANOWSKI AND ANAND GNANADESIKAN

Geophysical Fluid Dynamics Laboratory/NOAA and AOS Program, Princeton University, Princeton, New Jersey

(Manuscript received 13 August 1997, in final form 13 January 1998)

ABSTRACT

Ocean simulations are in part determined by topographic waves with speeds and spatial scales dependent on bottom slope. By their very nature, discrete *z*-level ocean models have problems accurately representing bottom topography when slopes are less than the grid cell aspect ratio $\Delta z/\Delta x$. In such regions, the dispersion relation for topographic waves is inaccurate. However, bottom topography can be accurately represented in discrete *z*-level models by allowing bottom-most grid cells to be partially filled with land. Consequently, gently sloping bottom topography is resolved on the scale of horizontal grid resolution and the dispersion relation for topographic waves is accurately approximated. In contrast to the standard approach using full cells, partial cells imply that all grid points within a vertical level are not necessarily at the same depth and problems arise with pressure gradient errors and the spurious diapycnal diffusion. However, both problems have been effectively dealt with. Differences in flow fields between simulations with full cells and partial cells can be significant, and simulations with partial cells are more robust than with full cells. Partial cells provide a superior representation of topographic waves when compared to the standard method employing full cells.

1. Introduction

There are at present three main strategies for building ocean general circulation models. Each centers around a different way of discretizing the vertical coordinate. The first involves discretizing a vertical column of ocean into levels. The vertical levels may have differing thickness but all grid points within a given level are at the same depth. The most widely used family of these *z*-level models is based on Bryan (1969) with the most recent member[1] being the Geophysical Fluid Dynamics Laboratory (GFDL) Modular Ocean Model (MOM) 2. Apart from the simplicity and computational efficiency of a *z*-level discretization, it has the advantage that accurate pressure gradients are easy to calculate, a nonlinear equation state may easily be included, and regions of weak stratification are easily modeled. The disadvantages are that topographic gradients less than the grid aspect ratio and bottom boundary layers are not well resolved unless very high vertical resolution is used, which in most cases is not feasible. Additionally, steep topographic gradients greater than the grid aspect ratio are not resolved unless very high horizontal resolution is used.

A second approach is to build a vertical coordinate from stratification by dividing the water column into layers of constant density. Such isopycnal coordinate ocean models (Bleck and Smith 1990; Hallberg 1995) can accurately approximate any topography. However, they are not able to easily handle a nonlinear equation of state and resolution degrades when density stratification is weak.

A third approach is to divide the water column into a fixed number of vertical regions with each being assigned some fraction of the total depth. These are the sigma-coordinate models (Blumberg and Mellor 1987; and Haidvogel et al. 1991), which can also accurately approximate any topography. However, they can have problems with ''pressure gradient errors'' and spurious diapycnal diffusion in regions where the bottom slopes steeply.

Gerdes (1993) attempted to resolve the inability of the *z*-level model to accurately incorporate topography by constructing a ''hybrid'' model, where the bottom level was a sigma surface, but the interior levels were at constant depths. Although he obtained substantial improvement in topographic wave propagation, he did not find an easy way to remove pressure gradient errors or spurious diapycnal diffusion in regions of steep topography.

Recently, Adcroft et al. (1997) proposed a finite-vol-

[1] Approximately 350 researchers are officially registered to use the GFDL MOM with about 130 officially registered to use the most recent version GFDL MOM 2 (Pacanowski 1996).

Corresponding author address: Ronald C. Pacanowski, NOAA/GFDL/AOS, Princeton University, P.O. Box CN710, Princeton, NJ 08540.
E-mail: rcp@gfdl.gov

ume approach using a *z*-level model based on a C-grid discretization in which the bottom-most cells were ''shaved'' to fit the topography. The shaving was quite general and could be applied to any or all faces of a grid cell thereby resolving lateral as well as bottom boundaries. He also compared this method to a special form of shaving, which kept the bottom cell faces horizontal. To our knowledge, this method was first explored by M. Cox (now deceased) over a decade ago but his results were never published, and according to M. Cox (1987, personal communication) the model was dropped because of being overly complex. We also suspect that Cox was discouraged over the resulting pressure gradient errors. In this paper, we explore the improvement in response resulting from a partial cell approach, which minimizes both pressure gradient errors and spurious diapycnal diffusion. This approach has been added as an option to the GFDL MOM 2, which is a discrete *z*-level model based on a B-grid discretization. No attempt has been made to better approximate lateral boundaries. Essentially, the partial cell approach represents a ''piecewise-sigma'' coordinate, which is embedded within each model level. Therefore, slow variations in topography are treated using the piecewise-sigma coordinate and rapid variations with the level coordinate. This is distinct from a true sigma coordinate model where sigma levels are continuous from the surface to the bottom of the ocean.

It is important to state that the partial cell method is not intended to capture the downslope flow associated with dense overflows such as the Denmark Straits, Faeroe Bank Channel, or Straits of Gibraltar. The reason is that the thickness of the bottom cell in many locations will exceed the thickness of the Ekman layer. As a result, stress-driven dynamics will not dominate over pressure gradient forces, and water that does flow downslope will experience high levels of entrainment as discussed by Winton et al. (1998) and also Baringer and Price (1997). An explicit parameterization of the bottom boundary layer such as given in Gnanadesikan (1998, manuscript submitted to *J. Phys. Oceanogr.*, hereafter G98) can remedy this problem. Beckmann and Doescher (1997) have also added a bottom boundary layer but their formulation, unlike G98 and the one proposed by Killworth and Edwards (1998, manuscript submitted to *J. Phys. Oceanogr*.), is not energetically consistent.

The structure of this paper is as follows: section 2 compares the ability of the partial cell and full cell to resolve bottom topography. Section 3 discusses the implementation of partial cells within a B-grid with emphasis on advection, diffusion, pressure gradients, and the equation of state. Energetic consistency for partial cells on a B-grid is demonstrated in the appendix. Section 4 considers wave propagation over a sloping bottom in an idealized zonally re-entrant channel. Section 5 compares the use of partial cells and full cells on a simulation of the Indian Ocean using a vertical discretization with 15 vertical levels and realistic topography. Section 6 concludes by summarizing the results.

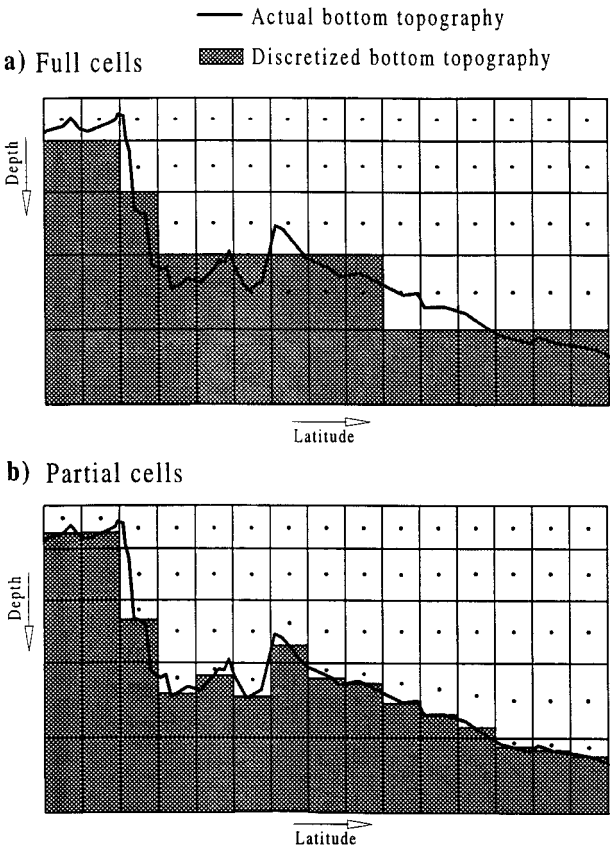

FIG. 1. An example comparing actual and discretized bottom topography for a given horizontal resolution: (a) using full cells and (b) using partial cells.

2. Resolving bottom topography

In the standard implementation of GFDL MOM 2, topography is discretized by finding the nearest vertical model level that most closely matches the depth of the topography at each longitude and latitude grid point within the model domain. The ocean bottom is then defined in terms of the number of vertical levels (grid cells) from the ocean surface down to this deepest ocean level. Figure 1a is an example of a typical section of bottom topography compared with the resulting discretized bottom. The solid line represents the ''true'' bottom, which the full cell discretization is trying to capture. Ocean cells within vertical levels are indicated with grid points and land cells are shaded. The partial cell discretization is indicated in Fig 1b where the bottom-most ocean cell in each column is partially filled with land while keeping the bottom cell face horizontal. Note that topography is significantly better approximated when partial cells are used. Most of the change in regions of steep slopes is captured by changes in the

number of vertical levels. Even so, partial cells give a better estimation of the true slope in these regions as well.

In regions where bottom slope is less than grid cell aspect ratio ($\Delta z/\Delta x$ or $\Delta z/\Delta y$), there are serious problems with full cells. Either these regions are entirely missed or are erroneously compressed into a steep slope separating regions with zero slope. The reason is that full cells capture slopes by forcing a change in the number of vertical levels between the surface and the ocean bottom. The latitude and longitude where a change in the number of levels occurs is determined by vertical grid resolution. Therefore, changing vertical resolution causes the location of these erroneous steep slopes to move! Partial cells have no such problems. Note how grid points follow the topography in Fig 1b. In effect, a piecewise sigma coordinate has been added within each vertical level by partial cells. The sigma coordinate is piecewise continuous because it is disconnected between vertical levels. For instance, horizontal gradients (i.e., pressure gradients) within a vertical level are constrained to work only with grid points within the level and not with grid points from other levels.

The case where horizontal resolution in Fig 1 is doubled but vertical resolution remains unchanged is given in Fig 2. Comparing Fig. 1a and Fig. 2a indicates that full cell discretized bottom topography does not significantly improve with increasing horizontal resolution. In fact, it remains about the same. In contrast, Fig. 1b and Fig. 2b indicates that the partial cell representation of topography continues to improve as horizontal resolution is increased. Note that the region of steepest slope would require still higher horizontal resolution to be accurately resolved. Since partial cells allow infinite resolution of topography in the vertical, topographic features are guaranteed to be resolved at the scale of the horizontal grid size. In practice, the minimum thickness of a partial cell should be limited to prevent transmitting information farther than one grid cell width in one timestep. This is not a problem for vertical velocity at the base of T-cells (tracer cells) (because the boundary condition is a zero vertical velocity on the bottom face of all deepest ocean T-cells) but can be for vertical velocity at the base of U-cells (velocity cells) (vertical velocity is related to the topographic slope at the base of U-cells). For simulations in this study, a minimum thickness of 5 m was used for partial cells unless otherwise noted. In general, for a fixed vertical resolution, as horizontal resolution increases, differences between full cell and partial cell topographic slopes grow larger. Clearly, along with topographic slopes, lines of constant f/H and the ocean volume as well are better approximated with partial cells.

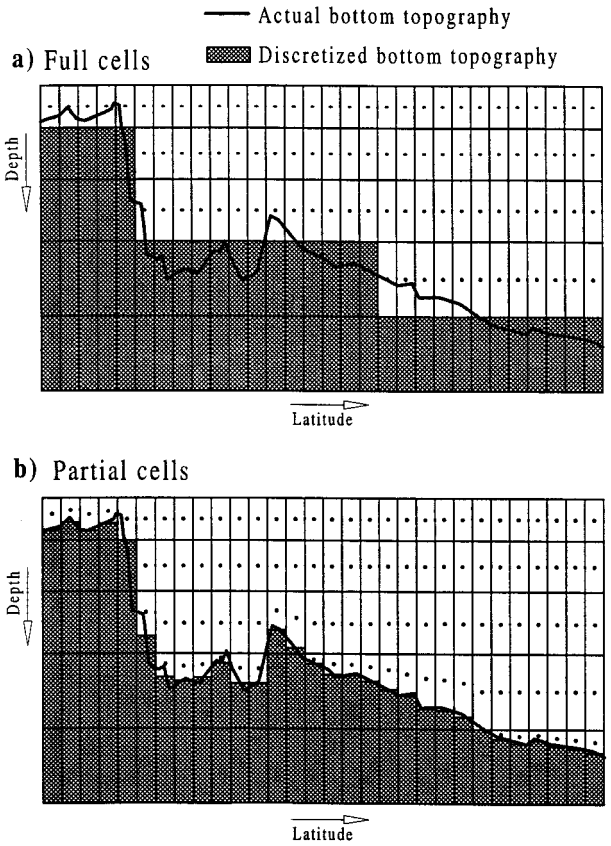

FIG. 2. An example comparing actual and discretized bottom topography using the same number of vertical levels but twice the horizontal resolution of Fig. 1. (a) using full cells and (b) using partial cells.

3. Implementing partial cells within a B-grid model

In the GFDL MOM 2 and its predecessors, resolution along any coordinate direction was only allowed to be a function of position along that coordinate. If this condition is relaxed to allow deepest ocean cells to have arbitrary thickness, then a partial cell bottom results where vertical cell thickness additionally becomes a function of latitude and longitude. To account for this generalization in the discrete equations, the area of each cell face must be taken into account when fluxing quantities cross a cell face. However, since the generalization is made only for the vertical coordinate, only the effective height of a cell face is necessary. The essential point is to approximate horizontal advective and diffusive operators by accounting for changes in cell thickness. A prescription for implementing this information into the finite-difference primitive equations (Bryan 1969) is given next.

Let the size of a grid volume element in spherical coordinates (λ, ϕ, z) on an Arakawa staggered B-grid for a T-cell and U-cell be represented as

$$(\Delta x^{\mathrm{T}} \cos\phi^{\mathrm{T}}, \Delta y^{\mathrm{T}}, \Delta h^{\mathrm{T}}) = (a\Delta\lambda^{\mathrm{T}} \cos\phi^{\mathrm{T}}, a\Delta\phi^{\mathrm{T}}, \Delta z^{\mathrm{T}}) \quad (1)$$

$$(\Delta x^{\mathrm{U}} \cos\phi^{\mathrm{U}}, \Delta y^{\mathrm{U}}, \Delta h^{\mathrm{U}}) = (a\Delta\lambda^{\mathrm{U}} \cos\phi^{\mathrm{U}}, a\Delta\phi^{\mathrm{U}}, \Delta z^{\mathrm{U}}), \quad (2)$$

where a is the radius of the earth and the superscripts refer to T-cells and U-cells. In general, the grid cell size

along any principle direction (longitude, depth, or latitude) is a function of position along that direction but not of the orthogonal directions. On the discrete grid, principal directions are discretized by index "*i*," which increases with longitude; "*k*," which increases with depth; and "*j*," which increases with latitude. For any tracer α defined at the grid point within a T-cell, the discrete prognostic equation in terms of full cell advective operator Adv(α) and diffusive operator Diff(α) is given by:

$$\delta_t(\alpha) = -\mathrm{Adv}(\alpha^\tau) + \mathrm{Diff}(\alpha^{\tau-1}) \tag{3}$$

$$\mathrm{Adv}(\alpha) = \frac{1}{\cos\phi^{\mathrm{T}}}\delta_\lambda(U_{t-1}\overline{\alpha_{t-1}}^{\lambda}) + \frac{1}{\cos\phi^{\mathrm{T}}} \times \delta_\phi(V_{j-1}\cos\phi^{\mathrm{U}}_{j-1}\overline{\alpha_{j-1}}^{\phi}) + \delta_z(W_{k-1}\overline{\alpha_{k-1}}^{z}) \tag{4}$$

$$\mathrm{Diff}(\alpha) = \frac{1}{\cos^2\phi^{\mathrm{T}}}\delta_\lambda(A_h\delta_\lambda\alpha_{t-1}) + \frac{1}{\cos\phi^{\mathrm{T}}} \times \delta_\phi(A_h\cos\phi^{\mathrm{U}}_{j-1}\delta_\phi\alpha_{j-1}) + \delta_z(\kappa\delta_z\alpha_{k-1}) \tag{5}$$

$$U = \overline{u_{j-1}\Delta y^{\mathrm{U}}_{j-1}}^{\phi}/\Delta y^{\mathrm{T}} \tag{6}$$

$$V = \overline{v_{i-1}\cos\phi^{\mathrm{U}}\Delta x^{\mathrm{U}}_{i-1}}^{\lambda}/\Delta x^{\mathrm{T}} \tag{7}$$

$$\delta_z(W_{k-1}) = -\frac{1}{\cos\phi^{\mathrm{T}}}(\delta_\lambda U_{i-1} + \delta_\phi V_{j-1}), \tag{8}$$

where only indices other than *i*, *k*, *j* are exposed to aid readability. At land boundaries, an insulating condition is used (i.e., the normal gradient of any tracer at the boundary is set to zero with the aid of masking arrays, which are not shown.). In the above equations, u and v are prognostic zonal and meridional velocities defined within U-cells, A_h and κ are horizontal and vertical diffusion coefficients, and U, V, and W are face-centered advective velocities for T-cells. For clarity, the arrangement of variables and indices on an Arakawa B grid is given in Fig. 3. The finite-difference derivative and average operators for any quantity β within a grid cell with subscripts *i*, *k*, *j* are expanded with all indices exposed as

$$\delta_\lambda\beta \equiv \delta_\lambda(\beta_{i,k,j}) = (\beta_{i+1,k,j} - \beta_{i,k,j})/\Delta x \tag{9}$$

$$\delta_\phi\beta \equiv \delta_\phi(\beta_{i,k,j}) = (\beta_{i,k,j+1} - \beta_{i,k,j})/\Delta y \tag{10}$$

$$\delta_z\beta \equiv \delta_z(\beta_{i,k,j}) = (\beta_{i,k,j} - \beta_{i,k+1,j})/\Delta z \tag{11}$$

$$\delta_t\beta \equiv \delta_t(\beta^\tau) = (\beta^{\tau+1} - \beta^{\tau-1})/2\Delta\tau \tag{12}$$

$$\overline{\beta}^{\lambda} \equiv \overline{\beta_{i,k,j}}^{\lambda} = (\beta_{i+1,k,j} + \beta_{i,k,j})/2 \tag{13}$$

$$\overline{\beta}^{\phi} \equiv \overline{\beta_{i,k,j}}^{\phi} = (\beta_{i,k,j+1} + \beta_{i,k,j})/2 \tag{14}$$

$$\overline{\beta}^{z} \equiv \overline{\beta_{i,k,j}}^{z} = (\beta_{i,k+1,j} + \beta_{i,k,j})/2, \tag{15}$$

where time is discretized as $\tau = n\Delta\tau$ for positive values of integer n and discrete time step size $\Delta\tau$. Operators can be applied to any grid cell. For example, a longitudinal average of a quantity β defined at the grid point within cell $i-1$, k, j is given by $\overline{\beta_{i-1,k,j}}^{\lambda} = (\beta_{i,k,j} + \beta_{i-1,k,j})/2$. Note that $\overline{\beta_{i-1,k,j}}^{\lambda}$ is defined at the eastern face of cell $i-1$, k, j, which is coincident with the western face of cell *i*, *k*, *j*. Within derivative operators, the grid spacing Δx, Δy, and Δz is symbolic. Actual grid spacing must be chosen with regard to where the quantity within the derivative is defined. In Fig. 3a, for example, the derivative $\delta(U_{i-1,k,j}) = (U_{i,k,j} - U_{i-1,k,j})/\Delta x^{\mathrm{T}}_i$ but $\delta(\alpha_{i,k,j}) = (\alpha_{i+1,k,j} - \alpha_{i,k,j})/\Delta x^{\mathrm{U}}_i$. The corresponding T-cell operators for partial cells are given by:

$$\mathrm{Adv}(\alpha) = \frac{1}{\Delta h^{\mathrm{T}}\cos\phi^{\mathrm{T}}}\delta_\lambda(U'_{i-1}\overline{\alpha_{i-1}}^{\lambda}) + \frac{1}{\Delta h^{\mathrm{T}}\cos\phi^{\mathrm{T}}} \times \delta_\phi(V'_{j-1}\cos\phi^{\mathrm{U}}_{j-1}\overline{\alpha_{j-1}}^{\phi}) + \delta_z(W_{k-1}\overline{\alpha_{k-1}}^{z}) \tag{16}$$

$$\mathrm{Diff}(\alpha) = \frac{1}{\Delta h^{\mathrm{T}}\cos^2\phi^{\mathrm{T}}}\delta_\lambda(\zeta^{\mathrm{T}}_{i-1}A_h\delta_\lambda\alpha_{i-1}) + \frac{1}{\Delta h^{\mathrm{T}}\cos\phi^{\mathrm{T}}} \times \delta_\phi(\zeta^{\mathrm{T}\phi}_{j-1}A_h\cos\phi^{\mathrm{U}}_{j-1}\delta_\phi\alpha_{j-1}) + \delta_z(\kappa\delta_z\alpha_{k-1}) \tag{17}$$

$$U' = \overline{u_{j-1}\Delta h^{\mathrm{U}}_{j-1}\Delta y^{\mathrm{U}}_{j-1}}^{\phi}/\Delta y^{\mathrm{T}} \tag{18}$$

$$V' = \overline{v_{i-1}\cos\phi^{\mathrm{U}}\Delta h^{\mathrm{U}}_{i-1}\Delta x^{\mathrm{U}}_{i-1}}^{\lambda}/\Delta x^{\mathrm{T}} \tag{19}$$

$$\delta_z(W_{k-1}) = -\frac{1}{\Delta h^{\mathrm{T}}\cos\phi^{\mathrm{T}}}(\delta_\lambda U'_{i-1} + \delta_\phi V'_{j-1}), \tag{20}$$

where Δh^{T} is the thickness of a T-cell as indicated in Fig. 3b. The variables $\zeta^{\mathrm{T}\lambda}$ and $\zeta^{\mathrm{T}\phi}$ are effective cell face heights defined as the minimum height of two adjacent T-cells in longitude and latitude, respectively. For longitude index *i*, latitude index *j*, and depth index *k*, the effective heights of the eastern face $\zeta^{\mathrm{T}\lambda}_{i,k,j}$ and northern face $\zeta^{\mathrm{T}\phi}_{i,k,j}$ of cell $T_{i,k,j}$ are given by:

$$\zeta^{\mathrm{T}\lambda}_{i,k,j} = \min(\Delta h^{\mathrm{T}}_{i,k,j}, \Delta h^{\mathrm{T}}_{i+1,k,j}) \tag{21}$$

$$\zeta^{\mathrm{T}\phi}_{i,k,j} = \min(\Delta h^{\mathrm{T}}_{i,k,j}, \Delta h^{\mathrm{T}}_{i,k,j+1}). \tag{22}$$

The lateral derivatives within Diff(α) need special attention and will be dealt with later. In comparison with Diff(α), the factors $\zeta^{\mathrm{T}\lambda}$ and $\zeta^{\mathrm{T}\phi}$ are missing from Adv(α) because they cancel the same factors, which otherwise would appear in the denominator of the right-hand-side of equations for U' and V'. Also, U' and V' are velocities weighted by the height of the cell face (that portion of the face that is in the ocean) on which they are defined in Eqs. (18) and (19) as opposed to simply face-centered velocities in Eqs. (6) and (7).

A similar set of operators exists for quantities within U-cells and the operations parallel those given for tracers. Since topography and geometry are constructed by material surfaces defined to lie on faces of T-cells, the vertical thickness of a U-cell with coordinate $U_{i,k,j}$ is given as the minimum of the four surrounding T-cell thicknesses:

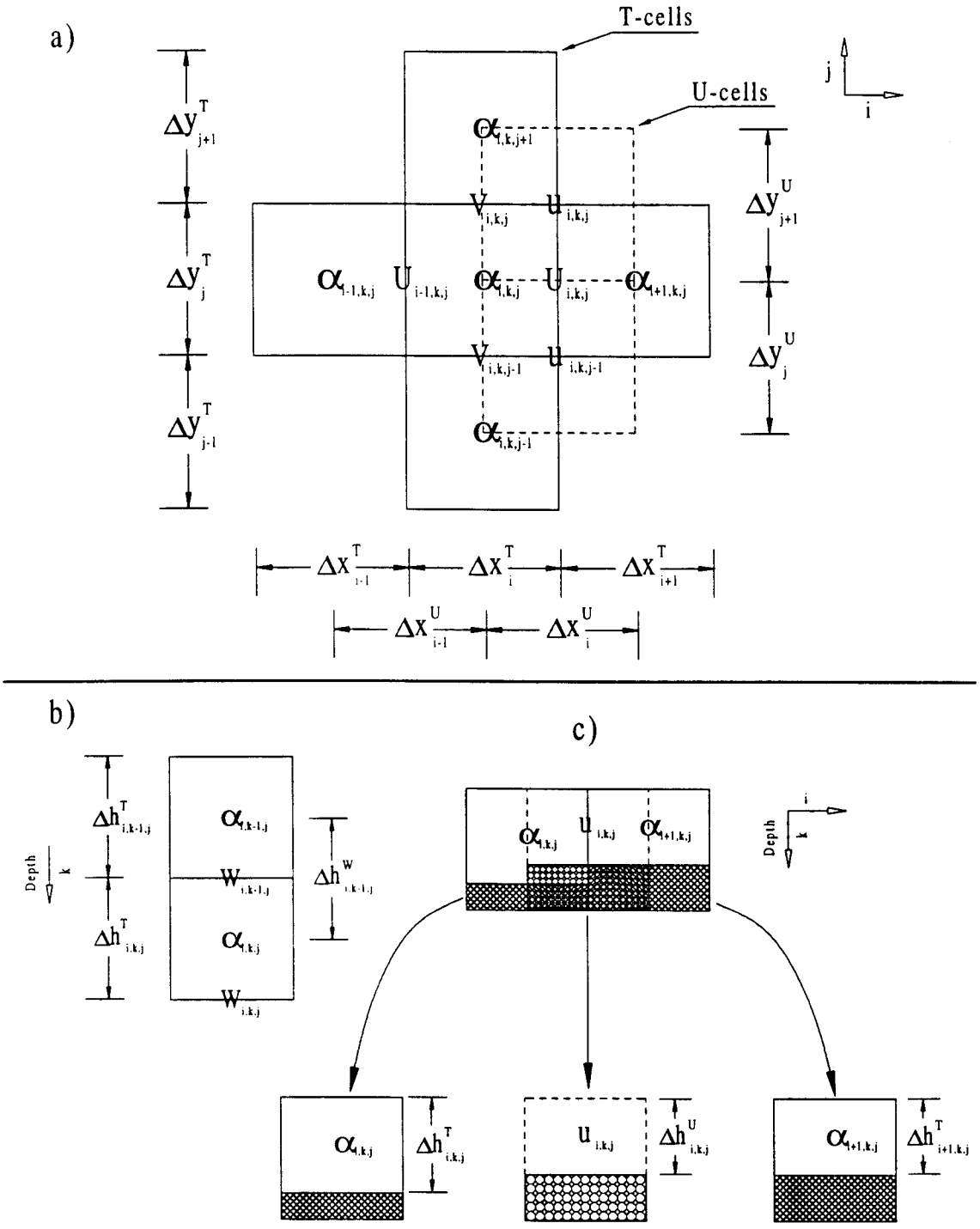

FIG. 3. Arrangement of variables and indices on an Arakawa B-grid including grid lengths that define the resolution of T-cells and U-cells. The longitudinal index is "*i*" and the latitudinal index is "*j*." The depth index is "*k*." (a) Arrangement in the horizontal plane. (b) Thickness of T-cells indicating vertical velocities at the top and bottom face. (c) Relationship between thickness of partial T-cells and U-cells in one dimension (longitude).

$$\Delta h^{U}_{i,k,j} = \min(\Delta h^{T}_{i,k,j}, \Delta h^{T}_{i+1,k,j}, \Delta h^{T}_{i,k,j+1}, \Delta h^{T}_{i+1,k,j+1}). \quad (23)$$

The relationship between thicknesses of partial T-cells and U-cells is illustrated along one dimension (longitude only) in Fig. 3c. Effective cell heights are also defined for the U-cells. For longitude index i, latitude index j, and depth index k, the effective heights of the eastern face $\zeta^{U\lambda}_{i,k,j}$ and northern face $\zeta^{U\phi}_{i,k,j}$ of cell $U_{i,k,j}$ are given by:

$$\zeta^{U\lambda}_{i,k,j} = \min(\Delta h^{U}_{i,k,j}, \Delta h^{U}_{i+1,k,j}) \quad (24)$$

$$\zeta^{U\phi}_{i,k,j} = \min(\Delta h^{U}_{i,k,j}, \Delta h^{U}_{i,k,j+1}). \quad (25)$$

Because the lateral boundary condition is no-flux for tracers but no-slip for velocity, the horizontal viscosity $h^{-1}\nabla \cdot (h\nabla(\mathbf{u}))$ has zonal and meridional components given by:

$$\begin{aligned}\text{Visc}^{\lambda} = {} & \frac{A_m}{\Delta h^{U} \cos^2\phi^{U}} \delta_{\lambda}(\zeta^{U\lambda}_{i-1} \delta_{\lambda} u_{i-1}) \\ & + \frac{A_m}{\Delta h^{U} \cos\phi^{U}} \delta_{\phi}(\cos\phi^{T}_{j-1} \zeta^{U\phi}_{j-1} \delta_{\phi} u_{j-1}) \\ & + A_m \frac{1 - \tan^2\phi^{U}}{a^2} u - A_m \frac{2 \sin\phi^{U}}{a^2 \cos^2\phi^{U}} \delta_{\lambda}(\overline{v_{i-1}}^{\lambda}) \\ & + S(u) \end{aligned} \quad (26)$$

$$\begin{aligned}\text{Visc}^{\phi} = {} & \frac{A_m}{\Delta h^{U} \cos^2\phi^{U}} \delta_{\lambda}(\zeta^{U\lambda}_{i-1} \delta_{\lambda} v_{i-1}) \\ & + \frac{A_m}{\Delta h^{U} \cos\phi^{U}} \delta_{\phi}(\cos\phi^{T}_{j-1} \zeta^{U\phi}_{j-1} \delta_{\phi} v_{j-1}) \\ & + A_m \frac{1 - \tan^2\phi^{U}}{a^2} v + A_m \frac{2 \sin\phi^{U}}{a^2 \cos^2\phi^{U}} \delta_{\lambda}(\overline{u_{i-1}}^{\lambda}) \\ & + S(v), \end{aligned} \quad (27)$$

where A_m is the lateral viscosity coefficient.[2] The above form differs from Bryan (1969) due to the inclusion of effective cell face heights $\zeta^{U\lambda}$ and $\zeta^{U\phi}$ and a sink term due to a no-slip lateral boundary condition. The sink terms is given by:

$$\begin{aligned} S(\beta) = {} & -\frac{A_m}{\Delta h^{U} \cos^2\phi^{U} \Delta x^{U}} \left[\frac{\Delta h^{U} - \zeta^{U\lambda}}{\Delta x^{T}_{i+1}} + \frac{\Delta h^{U} - \zeta^{U\lambda}_{i-1}}{\Delta x^{T}} \right] \beta \\ & - \frac{A_m}{\Delta h^{U} \cos\phi^{U} \Delta y^{U}} \left[\frac{\cos\phi^{T}_{j+1} (\Delta h^{U} - \zeta^{U\phi})}{\Delta y^{T}_{j+1}} \right. \\ & \left. + \frac{\cos\phi^{T} (\Delta h^{U} - \zeta^{U\phi}_{j-1})}{\Delta y^{T}} \right] \beta, \end{aligned} \quad (28)$$

which is zero where U-cell thickness is constant (i.e., $\Delta h^{U} = \zeta^{U\lambda}$) within a vertical level but acts as a bottom drag

$$S(\beta) \propto (A_m / \Delta^2 x^{U}) \beta \quad \cdots \text{ assuming } \Delta x^{U} = \Delta y^{U}, \quad (29)$$

where U-cell thickness varies within a vertical level. The constant of proportionality $[(\Delta h^{U} - \zeta^{U\lambda})/\Delta h^{U}]$ represents the fraction of cell face height over which a no-slip condition is applied. Again, subscripts have been suppressed except where different than i, k, j.

The advective terms for momentum are similar to the ones for advection of tracers except that effective cell face heights are for U-cells rather than for T-cells. In the interior, equations are second-order accurate (Treguier et al. 1996) but reduce to first order at bottom boundaries because the thickness of partial cells breaks the analytical-based stretching of grid cell thickness in the vertical. Although the equations drop from second order in the interior to first order for nonfull cells at the bottom, a leading-order error in the position of the topography has been corrected. Globally, the solution remains second-order accurate.

a. Horizontal pressure gradients

When density is only a function of depth $\rho(z)$, horizontal gradients of density at a constant depth are zero. The hydrostatic assumption implies that pressure p is proportional to the vertical integral of density and therefore horizontal pressure gradients at a constant depth are also zero (in the absence of barotropic pressure gradients). This is the case when using full cells because all grid points within any vertical level are at the same depth.

Partial cells complicate matters because all grid points within a vertical level are not necessarily at the same depth. The depth surface defined by grid points within a vertical level remains horizontally flat in the ocean interior but becomes deformed near land boundaries. This deformation of the depth surface must be taken into account by applying a correction when computing horizontal pressure gradients. Without loss of generality, consider only the zonal pressure gradient within a vertical level written in spherical coordinates as

$$\begin{aligned} & -\frac{1}{a \cos\phi \rho_o} \frac{\partial p}{\partial \lambda}\bigg|_{z=\text{constant}} \\ & \quad = -\frac{1}{a \cos\phi \rho_o} \left(\frac{\partial p}{\partial \lambda}\bigg|_{z^{T}(\lambda)} + \frac{\partial p}{\partial z}\bigg|_{z=\text{constant}} \frac{\partial Z^{T}(\lambda)}{\partial \lambda} \right), \end{aligned} \quad (30)$$

where $Z^{T}(\lambda)$ is the surface defined by the depth of grid points within a vertical level. The left-hand-side of Eq. (30) is the zonal pressure gradient evaluated along a surface that is locally flat. The first term on the right-hand-side of Eq. (30) is the pressure gradient along the surface $Z^{T}(\lambda)$ and the last term is a correction, which is nonzero only where the surface is not horizontal. The

[2] The formulation is for constant A_m. Variable A_m requires additional terms.

correction has a positive sign because $Z^T(\lambda)$ is measured as positive downward from the ocean surface, whereas the vertical coordinate z is positive upward. Substituting the hydrostatic assumption

$$p(z) = \int_z^0 \rho g \, dz' \tag{31}$$

into the right-hand-side of Eq. (30) yields:

$$-\frac{1}{a\cos\phi\rho_0}\frac{\partial p}{\partial\lambda}\bigg|_{z=\text{constant}} = -\frac{g}{a\cos\phi\rho_0}\left(\frac{\partial}{\partial\lambda}\left[\int_{Z^T(\lambda)}^0 \rho \, dz'\right] - \rho|_{z=\text{constant}}\frac{\partial Z^T(\lambda)}{\partial\lambda}\right), \tag{32}$$

where g is acceleration due to gravity, ρ_O is the mean ocean density, ρ is density, and the barotropic surface pressure gradient $\partial\rho_s/\partial\lambda$ has been dropped. The key point is that in a full cell discretization, $\partial Z^T(\lambda)/\partial\lambda = 0$ because the vertical coordinate does not vary with spatial position. In the partial cell case, a correction must be applied where cells become partial. Refer to Fig. 4, which illustrates two vertical columns of T-cells where the bottom cell in one of the columns is a partial cell and therefore grid points in level ''k'' are not all at the same depth. Let density ρ be defined at the grid points indicated by ''black dots'' with indexing as shown. In general, if density is a function of z only, there should be no horizontal pressure gradients and therefore no flow.

Let $\mathcal{P}_\lambda(k)$ represent the discretization of the right-hand-side of Eq. (32). In terms of grid distances and cells indicated in Fig. 4:

$$\mathcal{P}_\lambda(k) = -\frac{1}{\rho_0\cos\phi}(\delta_\lambda(p_{i,k}) - g\overline{\rho_{i,k}}^{\lambda}\delta_\lambda(zt_{i,k})), \tag{33}$$

where $zt_{i,k}$ is the depth of tracer grid points measured from the ocean surface. Discrete pressure $p_{i,k}$ is defined from the hydrostatic assumption as the vertical integral of ρg and gradients of pressure along the surface given by $zt_{i,k}$ for a constant vertical level index ''k'' are discretized as

$$\delta_\lambda(p_{i,k}) = g\Delta h^W_{i,0}\delta_\lambda(\rho_{i,1}) + g\delta_\lambda\left(\sum_{m=2}^{k}\overline{\rho_{i,m-1}}^{z}\Delta h^W_{i,m-1}\right). \tag{34}$$

As indicated in Fig. 4, the distance between a grid point at $zt_{i,k}$ and $zt_{i,k-1}$ is given by $\Delta h^W_{i,k}$. If it is assumed that $\rho = \rho(z)$, then $\mathcal{P}_\lambda(k)$ reduces to

$$\mathcal{P}_\lambda(k) = -\frac{g}{2\rho_0\cos\phi} \times\left(\overline{\rho_{i,k-1}}^{\lambda}\delta_\lambda(zt_{i,k}) + \overline{\Delta h^W_{i,k-1}}^{\lambda}\delta_\lambda(\rho_{i,k}) - \overline{\rho_{i,k}}^{\lambda}\delta_\lambda(zt_{i,k})\right), \tag{35}$$

which is zero when grid points within level k are all at the same depth. In general, $\mathcal{P}_\lambda(k) \neq 0$ if either cell at level k is a partial cell. However, if $\rho(z)$ is assumed to vary linearly with depth, the first two terms on the right-hand-side of Eq. (35) can be combined to equal the negative of the third term resulting in $\mathcal{P}_\lambda(k) = 0$. A proof of the energetic consistency of the pressure term with partial cells is given in the appendix.

b. Equation of state

We have just demonstrated that linear variations in density with depth will not result in pressure gradient errors. In GFDL MOM 2 and its predecessors, ρ is approximated as a deviation from a reference density, which is itself a function of depth. The reference density is based on horizontally averaged temperatures and salinities from the Levitus climatological atlas (1982) that have been interpolated to discrete depths of the grid points within full cell model levels. The density anomaly is computed as a third-order polynomial approximation to the UNESCO equation of state (Bryan and Cox 1972). Using the UNESCO formula directly is significantly more computationally expensive than the polynomial approximation; partly because UNESCO depends on in situ temperature, whereas the model uses potential temperature. The resulting polynomial coefficients and related reference data are only appropriate for use with potential temperature and salinity defined at the depth of grid points within discrete model levels.

Since pressure varies linearly with depth below a few hundred meters in the ocean, there is an error in trying to use this polynomial approximation at the grid points within partial cells. The reason is that grid points within partial cells are not at the same depth as full cell grid points within the same vertical level. As a result, density anomalies are in error and can drive spurious flows. Consider a linear stratification of temperature and salinity with depth in an ocean at rest and a nonlinear equation of state. There should be no motion. Yet, nonzero velocities that are not insignificant can spontaneously develop.

These error velocities are in part due to an incorrect estimation of the pressure effect with depth inside of partial cells; the other part is due to nonlinearities in the equation of state. By accounting for the actual depth of the grid point within partial cells, the maximum error velocity can be significantly reduced. Various methods were tried and gave essentially the same result. The method currently in use relies on the fact that the generated polynomial coefficients and reference data are independent of longitude, latitude, and time. They are only a function of depth. Referring to Fig. 4, the method amounts to vertically interpolating polynomial data defined at depths $zt_{i+1,k}$ and $zt_{i+1,k-1}$ to the depth of the open circle at $zt_{i,k}$. The interpolated coefficients and references are then used along with potential temperature

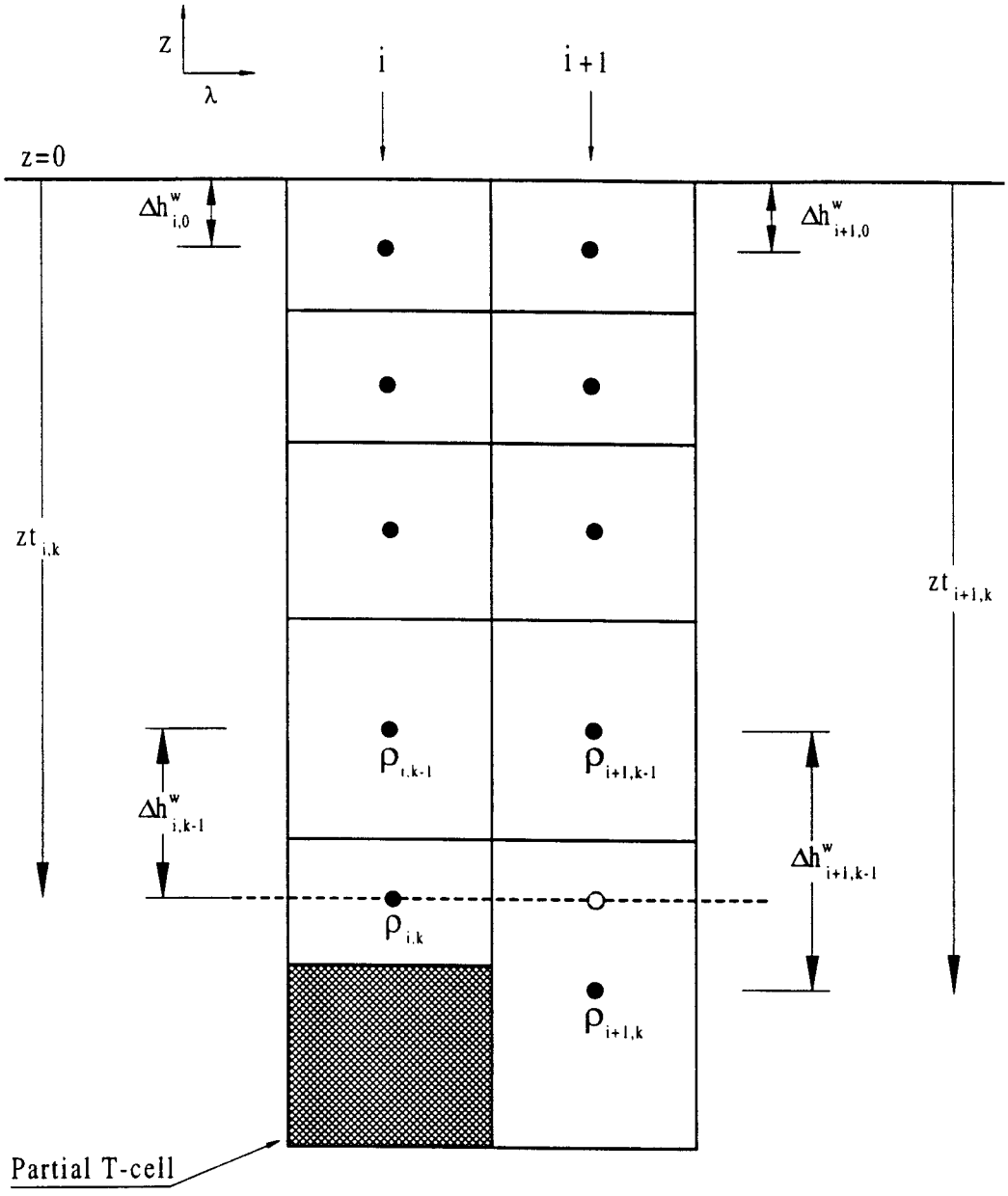

FIG. 4. Relationship between grid points, variables, and indices in partial cells and full cells. Two vertical columns of T-cells with one partial bottom cell indicated.

and salinity defined in the partial cell at the depth $zt_{i,k}$ to determine the density $\rho_{i,k}$.

Figure 5 is an example of spontaneously generated error velocities due to partial cells. A Gaussian topographic bump was placed within a rectangular domain 10° on a side with 1° horizontal resolution and nine vertical levels of uniform 500-m thickness (except for partial cells at the bottom). The fluid was linearly stratified (potential temperature varied from 25°C at $z = 0$ to 0°C at $z = 4500$ m with a salinity of 35 ppt) and initially at rest on an f plane at 45° N. With zero surface forcing and a zero vertical diffusion coefficient, the state of rest persists when using full cells but does not when using partial cells. The upper-left panel shows a slice through the center of the topographic rise. The magnitude of the error velocity using uncorrected density coefficients is given in the upper right panel for a depth of 3250 m after 25 days of integration. The maximum value is about 0.45 cm s^{-1}. The corresponding result using corrected density coefficients is given in the lower-left panel and a time history of the maximum error velocity magnitude at 3250 m for both cases is given in the lower-right panel. The maximum amplitude error velocity is reduced by an order of magnitude when using

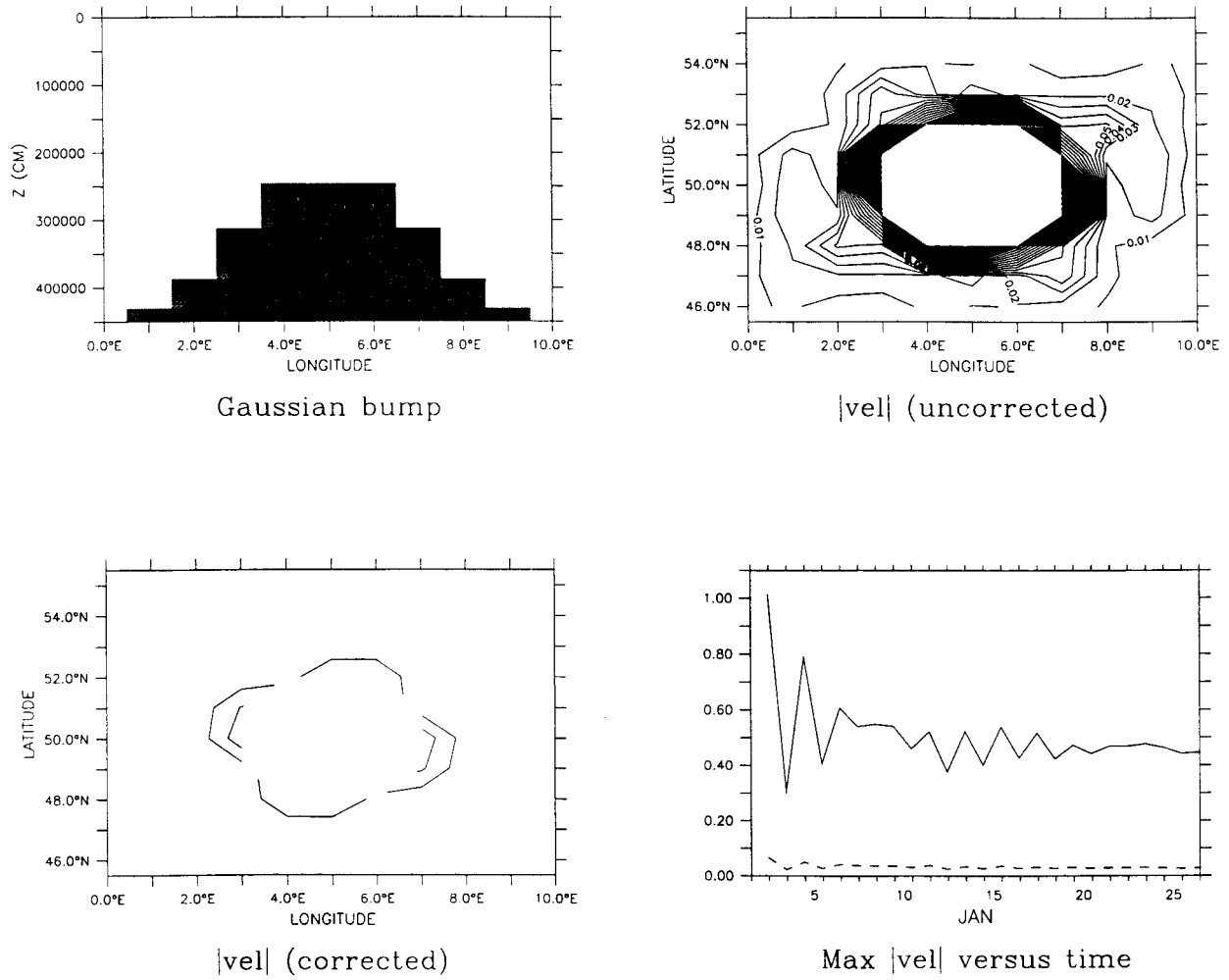

FIG. 5. (upper left) A longitudinal vs depth slice through a Gaussian-shaped bottom topography. (upper right) Magnitude of error velocity in cm s^{-1} at a depth of 3250 m after 25 days of integration with uncorrected density coefficients. Contour interval = 0.01 cm s^{-1}. (lower left): Magnitude of error velocity in cm s^{-1} at a depth of 3250 m after 25 days of integration with corrected density coefficients. Contour interval = 0.01 cm s^{-1}. (lower right) Maximum error velocity magnitude in cm s^{-1} at a depth of 3250 m for uncorrected (solid line) and corrected (dashed line) density coefficients as a function of time.

corrected density coefficients. Ultimately, the size of this error velocity depends on stratification and depth variations within partial cells.

It should be noted that in the level above a partial cell there is a zero pressure gradient error. Pressure gradient errors can exist only where levels intersect bottom topography. Compared to partial cells within GFDL MOM 2, a true ''sigma coordinate'' model will have pressure gradient errors in all levels above the bottom.

c. Spurious diffusion

As noted in the previous section, in the absence of forcing, a fluid at rest should remain at rest when density is a function of potential temperature $\rho = \rho(\alpha, z)$ and potential temperature α is a linear function of depth.[3] This is indeed the case in a discrete z-level model when full cells are employed, because at a fixed depth horizontal pressure gradients are zero and $\delta_\lambda(\alpha) = \delta_\phi(\alpha) = 0$ so lateral diffusion is also zero. If a bottom slope exists in a discrete z-level model, to ensure the fluid remains at rest, the vertical diffusivity coefficient must also be set to zero since $\delta_z(\alpha) = constant$ in the interior but $\delta_z(\alpha) = 0$ at the bottom boundary due to the insulating bottom boundary condition.

[3] In a laboratory experiment, fluid creep will result along sloping insulating sidewalls due to molecular motions. Apart from these motions, however, no motion should be introduced due to the numerical discretization of diffusion.

Since grid points within a constant depth level of partial cells follow the ocean terrain, lateral diffusion in the surface containing the grid points has a projection in the vertical resulting in spurious vertical (diapycnal) diffusion, which gives rise to horizontal pressure gradients and motion. This happens whenever coordinate surfaces are not aligned along surfaces of constant depth. Refer again to Fig. 4 and let tracer α be linearly stratified potential temperature discretized to grid points indicated by ''black dots'' with indexing the same as shown for ρ. Note that the horizontal derivative of temperature at level $k - 1$ is zero ($\delta_\lambda(\alpha_{i,k-1}) = 0$) but nonzero in the level containing the partial cell ($\delta_\lambda(\alpha_{i,k}) \neq 0$). Since a linear stratification with depth implies that temperature is colder with increasing depth, lateral diffusion will cause $\alpha_{i,k}$ to cool and $\alpha_{i,+1,k}$ to warm. This spurious diapycnal diffusion is initiated solely because grid points within the same vertical level are at different depths. Note that lateral mixing does not propagate this error across levels.

By using $\alpha_{i+1,k-1}$ and $\alpha_{i+1,k}$ to linearly interpolate temperature to the location of the ''open circle'' in Fig. 4 and using this interpolated value to construct a lateral diffusive flux in the diffusive operator Diff(α), the spurious diapycnal diffusion is largely eliminated. A similar vertical interpolation is not used for lateral viscous terms in the momentum equation because velocity components do not enter the density equation.

4. Stratified topographic waves in a channel

To explore the effect of a partial cell bottom on transient response, consider an idealized zonally re-entrant channel that is 10° long × 10° lat on an f plane at 45°N with a 1° horizontal resolution. The channel is 4500 m deep in the south and the bottom shallows northward at a rate of 100 m deg^{-1} to a depth of 3500 m in the north. There is no variation of ocean depth with longitude and there are nine vertical levels of constant 500-m thick in the vertical. In the partial cell channel, the bottom-most ocean cell is allowed to vary and becomes as thin as 50m. A latitude-depth section illustrating T-cells, grid points, and topography for the full cell and partial cell channel is given in Fig. 6. The gentle slope is resolved with partial cells but not with full cells. Note the artificial topographic ridges in the the full cell discretization, which are missing with partial cells.

If we assume linear, hydrostatic, Boussinesq equations,

$$\frac{\partial u}{\partial t} - fv = -\frac{1}{\rho_0}\frac{\partial p}{\partial x} \tag{36}$$

$$\frac{\partial v}{\partial t} + fu = -\frac{1}{\rho_0}\frac{\partial p}{\partial y} \tag{37}$$

$$\frac{\partial p}{\partial z} = -\rho g \tag{38}$$

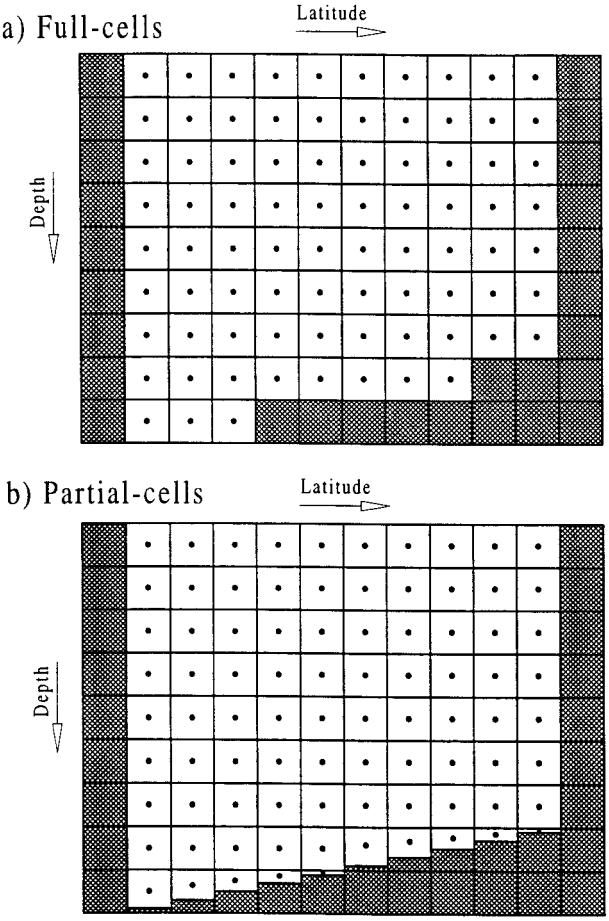

FIG. 6. A latitude vs depth slice through the zonally re-entrant channel indicating T-cells, grid points, and topography: (a) full cells and (b) partial cells.

$$\frac{\partial \rho}{\partial t} = -w\frac{\partial \rho}{\partial z} \tag{39}$$

$$\frac{\partial u}{\partial x} + \frac{\partial v}{\partial y} + \frac{\partial w}{\partial z} = 0 \tag{40}$$

and apply them to the re-entrant channel, then in the quasigeostrophic limit, the solution (Rhines 1970) is given in terms of propagating waves of the form

$$\rho = A \sin(kx - \omega t) \sin(n\pi y/L_y) \sinh(\lambda z), \tag{41}$$

where k is a zonal wavenumber. n is a meridional wavenumber, $L_y = 10°$, z is depth, and

$$\lambda = (k^2 + n^2\pi^2/L_y^2)^{1/2} = \frac{N}{f} \tag{42}$$

$$\omega = \frac{S_b k N^2}{f\lambda \tanh(\lambda D)}. \tag{43}$$

The phase speed for any of these waves is $c = \omega/k$, the topographic slope is S_b, and D is the depth of the slope. Initially there is no forcing, no motion, and the strati-

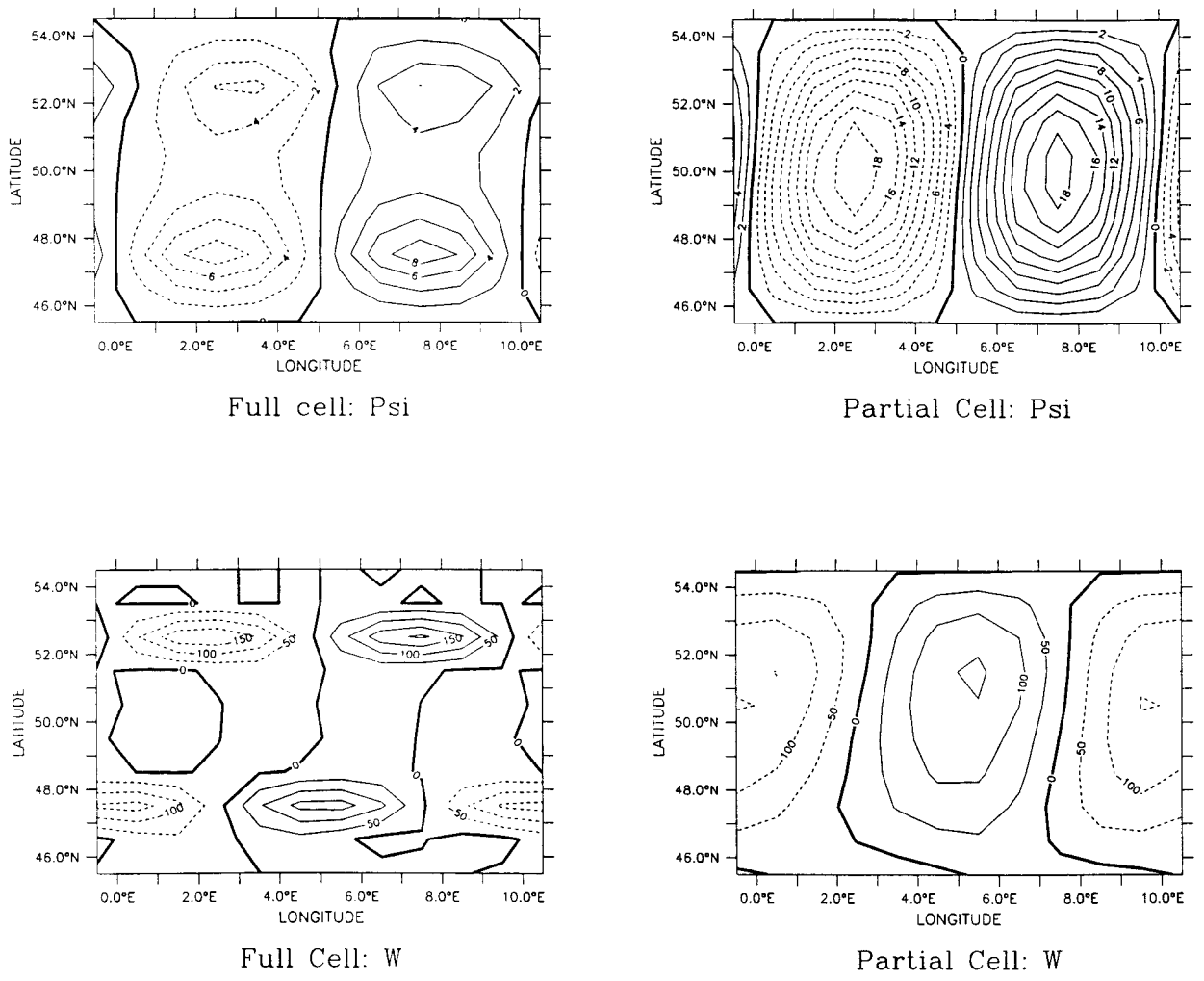

FIG. 7. Solution after 100 days of integration. (upper panels) Streamfunction in Sv. (lower panels) Vertical velocity at a depth of 3500 m in cm day^{-1}.

fication is a linear function of depth with a frequency given by $N = 0.003\ \text{s}^{-1}$.

In the first experiment, an initial density perturbation of the form

$$\rho = 0.5 \sin(2\pi x/L_x) \sin(\pi y/L_y) \tanh(\lambda z) \quad (44)$$

was introduced to initialize one of these topographic waves. GFDL MOM 2 was employed to solve the above system of equations using a full nonlinear equation of state, constant horizontal diffusion coefficients for tracers and momentum ($1 \times 10^7\ \text{cm}^2\ \text{s}^{-1}$), a vertical diffusion coefficient of $1.0\ \text{cm}^2\ \text{s}^{-1}$, a vertical viscosity coefficient of $20.0\ \text{cm}^2\ \text{s}^{-1}$, and a second-order centered advective scheme. Sidewall boundary conditions for momentum were no-slip and along the bottom a free-slip condition was used. The model was integrated for 100 days and instantaneous data were saved once per day. The upper panels in Fig. 7 show the horizontal streamfunction after 100 days of integration for two cases: one with a full cell bottom and the other with a partial cell bottom. Comparing streamfunctions, the initial perturbation in the full cell case has broken up into two double Kelvin waves, each running along a topographic ridge indicated in Fig 6a. By contrast, the partial cell case produces a signal which, like the initial perturbation, is dominated by a single maximum in the middle of the basin. Note that the amplitude of the streamfunction in the full cell case is substantially reduced in comparison to the amplitude in the partial cell case. This is because horizontal viscosity acts more strongly on smaller spatial scales than larger ones. The difference in spatial scale is also apparent in the vertical velocity fields at a depth of 3500 m as shown in the lower panels of Fig. 7. However, since vertical velocity is computed as the divergence of horizontal velocity, small horizontal spatial scales in the full cell case imply large vertical velocities with the same small horizontal scale. Therefore, where topographic slopes are resolved,

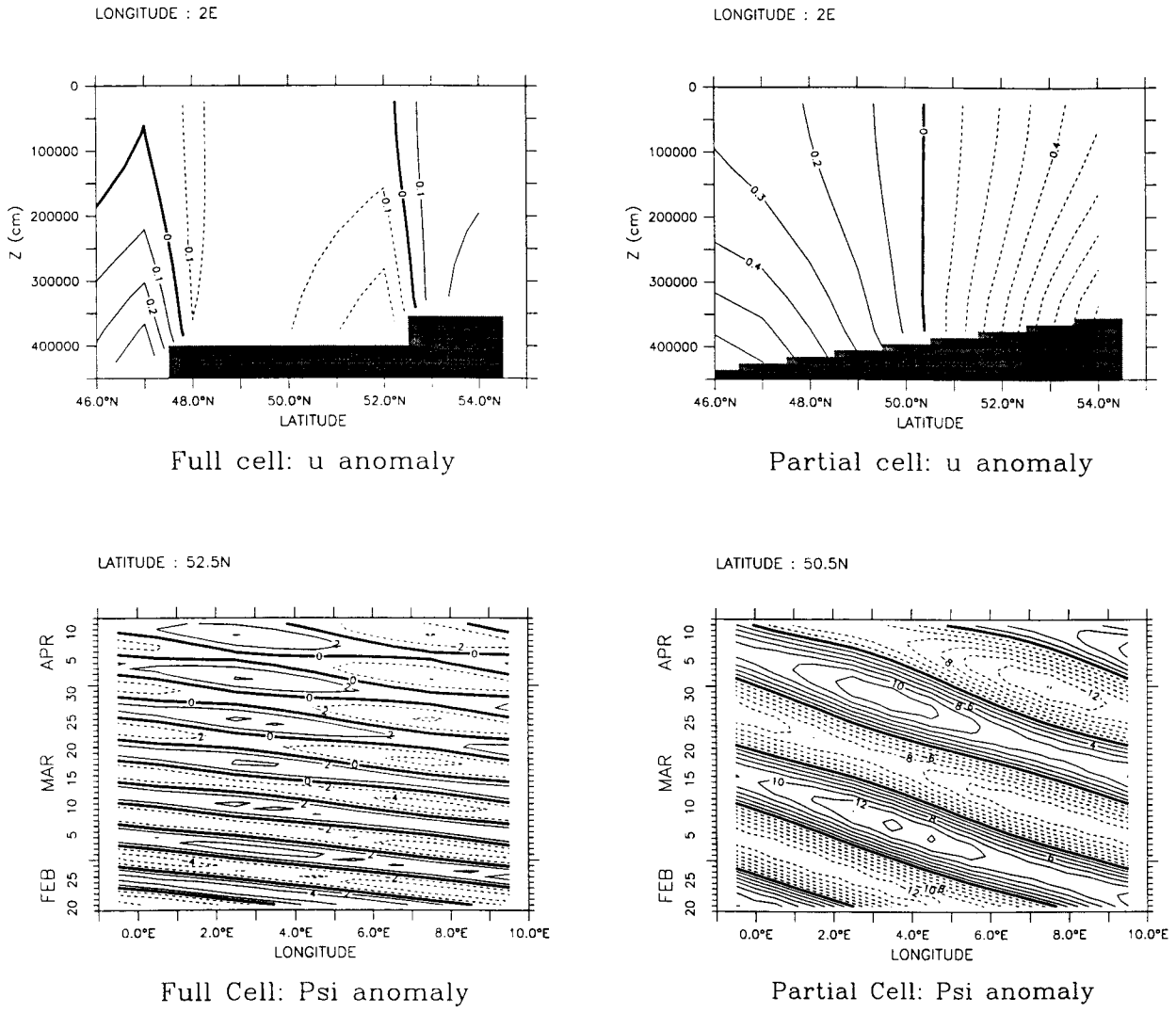

FIG. 8. Vertical structure and phase speed of a single wave after 100 days of integration. (upper panels) Vertical structure of the zonal velocity anomaly in cm s^{-1} after 100 days of integration. (lower panels) Phase speed of a single wave. Streamfunction anomaly in Sv as a function of longitude and time.

vertical velocity fields are smoother (less small-scale noise) with partial cells than with full cells.

A comparison of the vertical structure of the zonal velocity anomaly (time mean from last 50 days removed) is given in the upper panels of Fig. 8 and indicates significant baroclinic differences. In the full cell case, the wave has small meridional scale and is vertically trapped with a maximum at the bottom. In the partial cell case, the wave exhibits a larger meridional scale with less vertical trapping. The wave propagation is shown in the lower panels of Fig. 8 in terms of streamfunction anomaly (time mean from last 50 days removed). The phase speed of the wave in the full cell case is 109 cm s^{-1}, which implies a basin crossing time of about 7.5 days. By contrast, the phase speed of the wave in the partial cell case is 43 cm s^{-1}, extremely close to the theoretical value of 42 cm s^{-1} for a linear wave. The basin crossing time is about 21 days. The damping of the wave with time is apparent in the full cell case but not in the partial cell case. Again, this is a consequence of scale selectivity of horizontal viscosity.

In the next experiment, an initial density perturbation with 25 horizontal wavelengths was allowed to evolve from rest for 100 days in a re-entrant channel 100° wide. The resulting solution was Fourier transformed to extract frequencies and construct a dispersion relation. The dispersion relation for both full cell and partial cell cases along with the analytical result are plotted in Fig. 9. The partial cell case accurately approximates the analytic dispersion relation for topographic waves, whereas the full cell case does not. Additionally, at high wave-

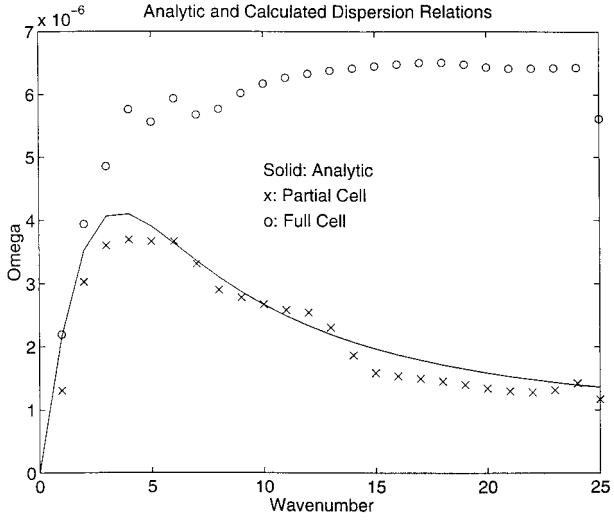

FIG. 9. Dispersion relation for topographic waves: analytical (solid line), partial cells (crosses), and full cells (open circles).

numbers, the full-cell dispersion relation has negligible group velocity and therefore does not propagate energy. To achieve the same accuracy as the model with partial cells, the full cell model would have required 20 levels of 50-m thickness between a depth of 3500 and 4500 m.

5. Simulating the Indian Ocean with full cells and partial cells

To test the effect of the partial cell bottom in a realistic domain, a 1° horizontal resolution version of the Indian Ocean was constructed. There are many places where partial cells might have an impact on the simulation of the World Ocean. In particular, areas such as the North Atlantic near the Labrador Sea, the far north in the Arctic basin, near Antarctica, the Pacific with its gentle east–west slope, marginal sea areas, or any other areas where the bottom slope is not resolved well by changes in vertical levels. The Indian Ocean was chosen because it has varied topography yet the domain is small enough and at a low enough latitude that the approach to equilibrium is relatively fast. If significant differences exist between full cell and partial cell simulations in this area, then it may reasonably be expected that partial cells will result in differences in the above-mentioned areas as well. These differences will be even more pronounced at higher latitudes where the influence of topography is larger due to a smaller Rossby radius in the ocean.

Vertical resolution was chosen to resolve the upper 100 m with an arbitrary specification of four uniformly thick 25-m levels. Below 100 m, vertical resolution was stretched with a cosine function to a thickness of 975 m at a depth of 5600 m. The above specification resulted in 15 vertical levels between the ocean surface and 5600 m with the following thickness distribution: 25, 25, 25, 25, 34.6, 72.3, 144.7, 245.8, 367.5, 500, 632.5, 754, 855.3, 927.6, and 965.3 m. Using this distribution, topography was generated for the domain by averaging the National Geophysical Data Center's ETOPO5 dataset (ETOPO5 1988) onto a 1° horizontal grid resolution and discretizing to the nearest vertical level. The partial cell discretization is given in Fig. 10. Note the gentle slope of the topography in the Arabian Sea (15°N, 65°E) and Bay of Bengal (15°N, 90°E). For comparison, the discretized full cell version of the same topography with 15 vertical levels is shown in Fig. 11. Note the artificial compression of topographic slopes into regions of sharp gradients separated by flat basins.

As an initial condition, there was no motion and potential temperatures and salinities were taken from the Levitus atlas (1982) for January. A sponge zone was applied next to the artificial wall at the southern boundary where the solution was damped back to monthly varying data from Levitus (1982) on a timescale that varied linearly from 15 days at the wall to no damping at 5° away from the wall. The model was forced by monthly Hellerman and Rosenstein wind stress (1983) and the surface temperatures and salinities (those within level one) were damped back toward the monthly varying temperature and salinity from the Levitus atlas (1982) on a timescale of 30 days. Constant horizontal and vertical mixing was used: lateral viscosity and diffusivity coefficients were both set to 1×10^7 cm^2 s^{-1}, the vertical viscosity coefficient was 10 cm^2 s^{-1}, and the vertical diffusivity coefficient was 0.1 cm^2 s^{-1}. Integration was for five years using a second-order centered advection scheme and 9-point numerics for solving the streamfunction equation. Instantaneous data were saved every 10 days throughout the intergration. The streamfunction solution contains a null mode, which is dynamically unimportant and has been removed from the figures by applying a 3-point running mean filter in latitude and longitude. The simulation repeated itself after the third year and all results are shown for year five.

From previous results in the zonally re-entrant channel, it is anticipated that differences will exist between full cell and partial cell simulations in regions of gently sloping topography. The Arabian Sea and Bay of Bengal are two such regions. A 3-month average of the streamfunction starting in March of the fifth year is shown in Fig. 12. The upper-left panel is from the 15-level partial cell simulation and the lower-left panel is from the 15-level full cell simulation. These will be referred to as cases 15p and 15f. The maximum streamfunction value is roughly 6 Sv (Sv $\equiv 10^6$ m^3 s^{-1}) in both and, qualitatively, patterns are similar. However, quantitatively there are 50% differences in the Bay of Bengal near (86°E, 15°N) and (85°E, 6°N) and similar differences can be found in the Arabian Sea. Which simulation is more realistic?

We are not aware of any measurements that will definitively show which case is closer to reality. However, it can be demonstrated that the full cell simulation is

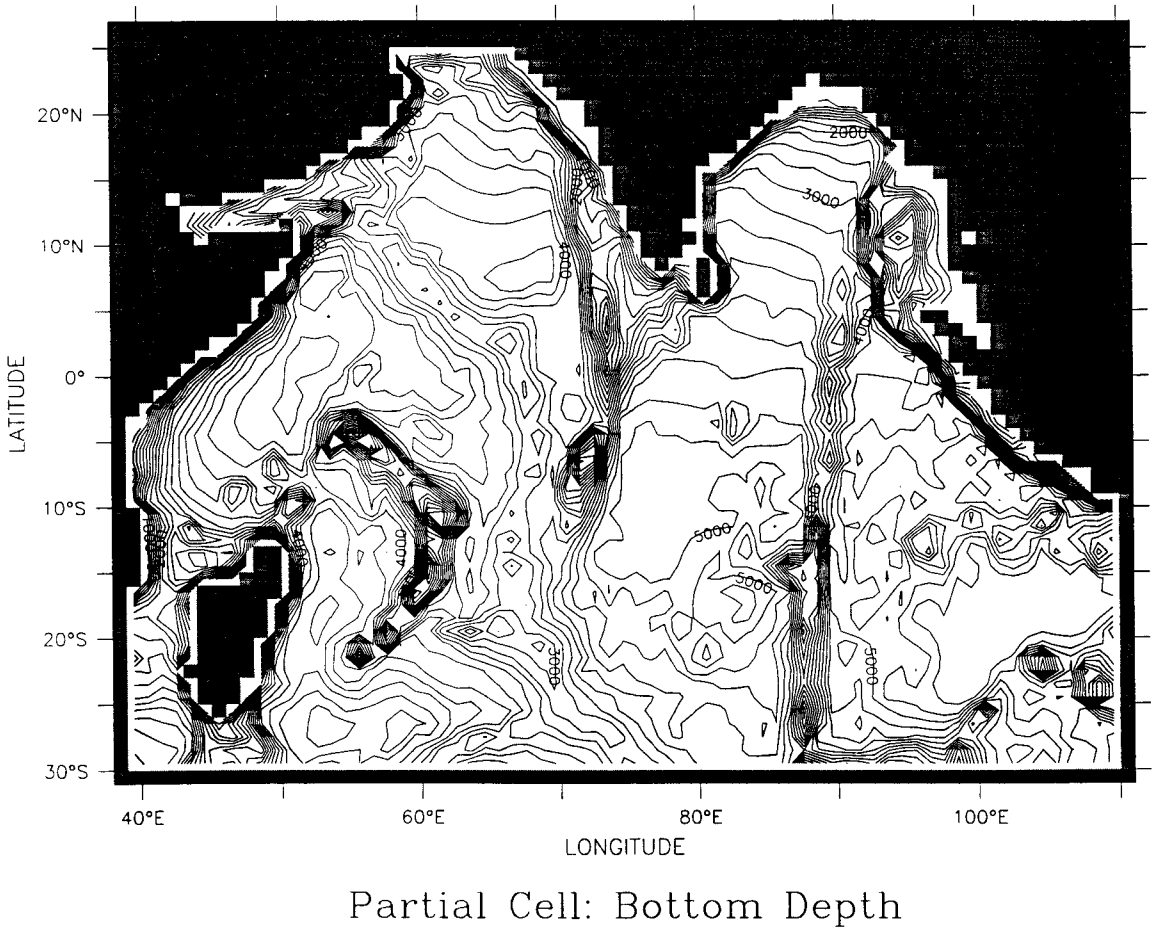

FIG. 10. Discretized topography defined on T-cells for the Indian Ocean basin using partial cells with a 1° horizontal resolution grid and 15 vertical levels. Contour interval is 250 m.

not as robust as the partial cell simulation by perturbing the vertical resolution from 15 to 16 levels and repeating the simulations with partial and full cells. The new simulations will be referred to as cases 16p and 16f. By adding one extra vertical level below 100 m, the ocean interior is not significantly better resolved; however, the positioning of the vertical levels is now different. As will be shown, this has implications for the discretized ocean bottom and the resulting simulations. The distribution of thickness for the 16 vertical levels was determined as before except that the vertical stretching was changed to give an 896.6-m thickness at 5600-m depth. This yielded 16 vertical levels with the following thickness distribution: 25, 25, 25, 25, 32.4, 61.4, 117.5, 196.8, 293.9, 402.3, 514.4, 622.7, 719.0, 799.2, 855.2, and 884.3 m.

The difference in streamfunctions between case 16p and case 15p is given in the upper-right panel of Fig. 12. The lower-right panel gives the difference between cases 16f and 15f. The difference in the full cell simulations is about four times greater than the difference in the partial cell simulations. A vertical section through the Arabian Sea along 62°E long is given in Fig. 13. A 3-month average of the amplitude of the horizontal velocity |**vel**| from the fifth year of integration is plotted for cases 15p and 15f along with differences from the 16-level simulations given as (case 16p minus case 15p) and (case 16f minus case 15f). To compute these differences, the 16-level results were linearly interpolated to the 15-level grid points before subtracting. It should be noted that the bottom-most gridpoint values in the partial cell cases are treated as if they were defined at the depth of the full cell grid points by the plotting program. This leads to an artificial stretching of isolines within deepest ocean grid cells. Results are consistent with the streamfunction differences indicating a lack of robustness for the full cells. However, the difference in the full cell simulations is substantially greater than four times the difference in partial cell simulations near the bottom. Although bottom flows are small, they represent nonnegligible water mass transport due to the large cross-sectional areas involved. Also, substantial differences in full cell cases extend well above the bottom.

The difference in the discretized bottom topography

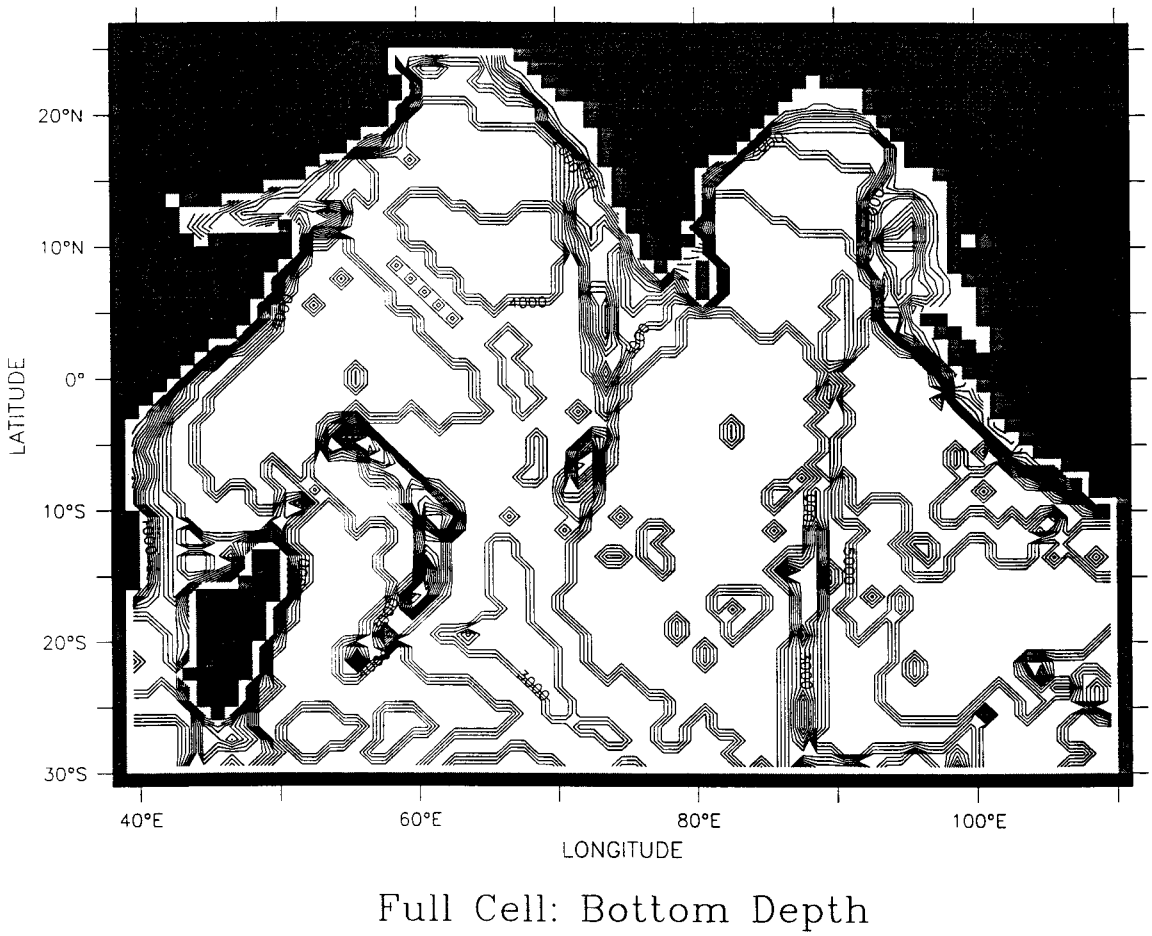

FIG. 11. Discretized topography defined on T-cells for the Indian Ocean basin using full cells with a 1° horizontal resolution grid and 15 vertical levels. Contour interval is 250 m. Some basin depths are as follows: the Arabian Basin (10°N, 65°E), Central Indian Basin (10°S, 80°E), and Somali Basin (0°N, 51°E) are 4635 m deep. The Bay of Bengal (8°N, 85°E) is 3707 m deep and the Cocos Basin (20°S, 100°E) is 5600 m deep.

between the 16-level and 15-level partial cell case is zero over most of the domain. At a few isolated locations, there is a difference of a few meters because of the restriction that no partial cell is allowed to be thinner than 5 m for computational reasons. The difference between the 16-level and 15-level full cell case is given in Fig. 14. Typically, at basin depths the differences (16 level minus 15 level case) are between 100 and 200 m. However, positive differences can be as large as 253 m and negative ones as large as −884 m. Both extremes can be found scattered randomly throughout the domain with spatial scales near the horizontal grid size.

The reason for a nonzero difference between the partial cell cases is illustrated in Fig. 15. Figures 15a and 15b depict how a sloping ocean bottom is discretized by two different distributions of vertical levels using full cells. Grid points within bottom-most ocean U-cells are connected by dashed lines (although the U-cells are not shown) and the discretized bottom is given by the depth from the ocean surface to the bottom face of the deepest ocean T-cells. In Fig. 15a, the bottom slope is compressed into two flat areas of different depth separated by a cliff and in Fig. 15b, the discretized bottom is completely flat and at a different depth than in Fig. 15a. Clearly, the discretized bottom depth is sensitive to the positioning of the bases of the vertical levels and is therefore not convergent with changes in vertical resolution. Figures 15c and 15d illustrate the case using partial cells. Note that the discretized bottom depth is convergent because it is the same in both Figs. 15c and 15d. However, the depth of the bottom-most ocean grid cell points is not convergent. Also note the discrete jump in bottom gridpoint depth where the bottom slope forces a change in levels as shown by the broken dashed line in Fig. 15d. Horizontal pressure gradients within bottom cells (defined at the open circles) will be different in Figs. 15c and 15d and result in differences of the magnitude shown in the upper-right panels of Figs. 12 and 13.

Moving toward the central and southern part of the

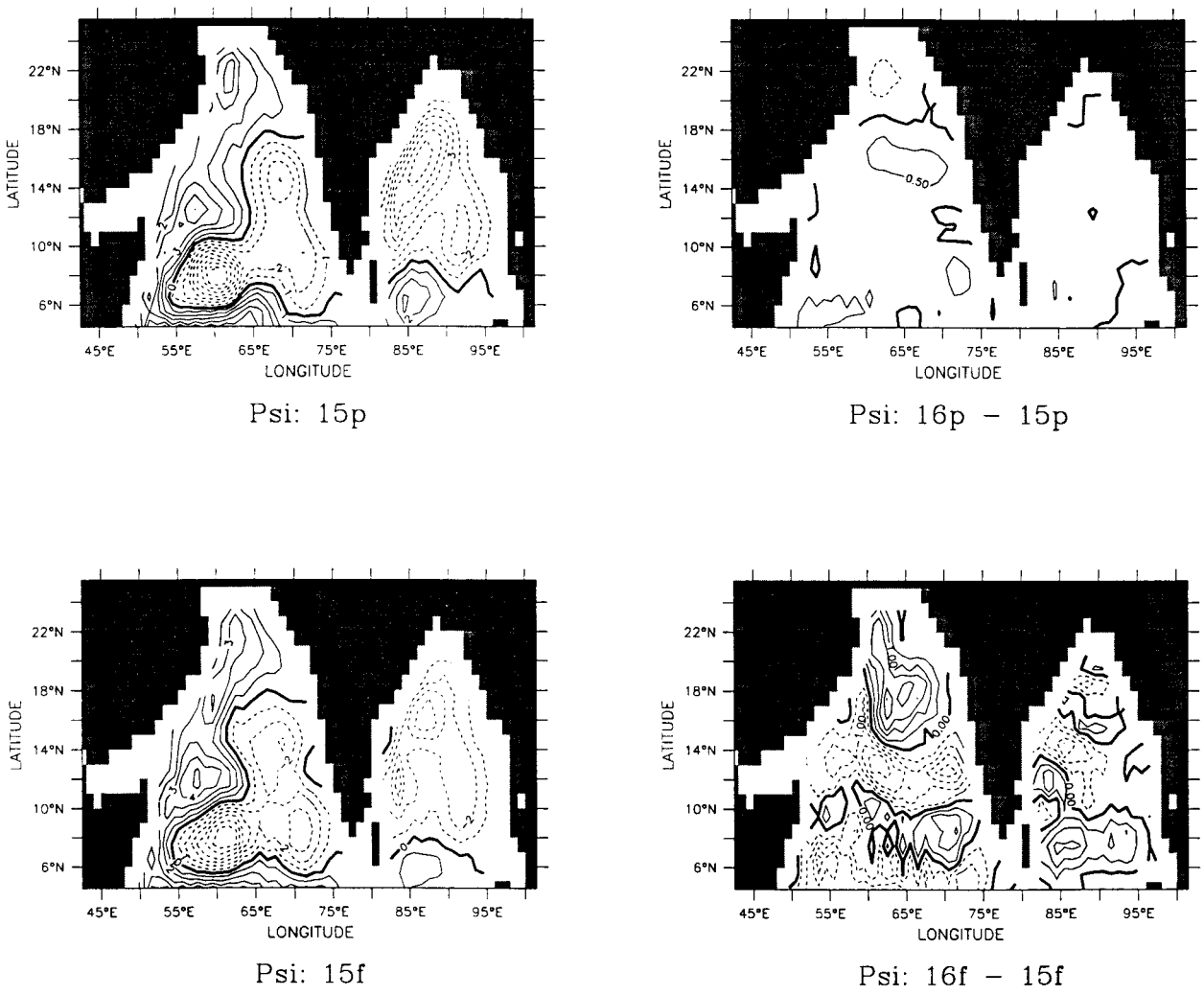

FIG. 12. Sensitivity in the horizontal streamfunction to changes in vertical levels in the northern part of the Indian Ocean. All results are for 3-month means from the spring of year 5. (upper left) Partial cell 15-level case. Contour interval is 1.0 Sv. (upper right) Partial cell 16-level case minus partial cell 15-level case. Contour interval is 0.5 Sv. (lower left) Full cell 15-level case. Contour interval is 1.0 Sv. (lower right) Full cell 16-level case minus full cell 15-level case. Contour interval is 0.5 Sv.

Indian Ocean bounded by the equator and latitude 30°S and longitudes 40°–90°E, the gentle slopes found in the north are replaced by more steeply varying topography. Since steep slopes are captured by changes in vertical levels rather than by piecewise continuous partial cells within a level, it is expected that the differences between full cell and partial cell simulations and the robustness of the partial cell simulations will not be as great as in the northern regions. Figure 16 gives the results for the streamfunction from a 3-month average in the spring of the fifth year for cases 15p and 15f along with the differences (case 16p minus case 15p) and (case 16f minus case 15f). The streamfunction reaches 30 Sv near 10°S, 45°E, which is about five times larger than in the northern areas. The difference in streamfunctions between 15f and 15p is about 5 Sv or only about 15% of the 30 Sv. This difference between full cell and partial cell simulations is much less than in the northern regions. The robustness of the partial cell solution has decreased relative to the northern region as indicated by larger contour values in the upper-right panel of Fig. 16. The worst area is near Madagascar (52°E, 20°S) where differences are 1.5 Sv on a streamfunction value of about 10 Sv. However, this is about the same percentage as in the Arabian Sea. East of the Madagascar Plateau (65°E, 20°S), there are similar differences over a broad area. The lower-right panel in Fig. 16 indicates that the differences between full cell cases are about twice those in the partial cell cases. Locally, there are many areas where the differences in full cell simulations exceed those in the partial cell simulations by more than a factor of two.

The root-mean-squared value of the streamfunction difference between cases 16p and 15p over the entire

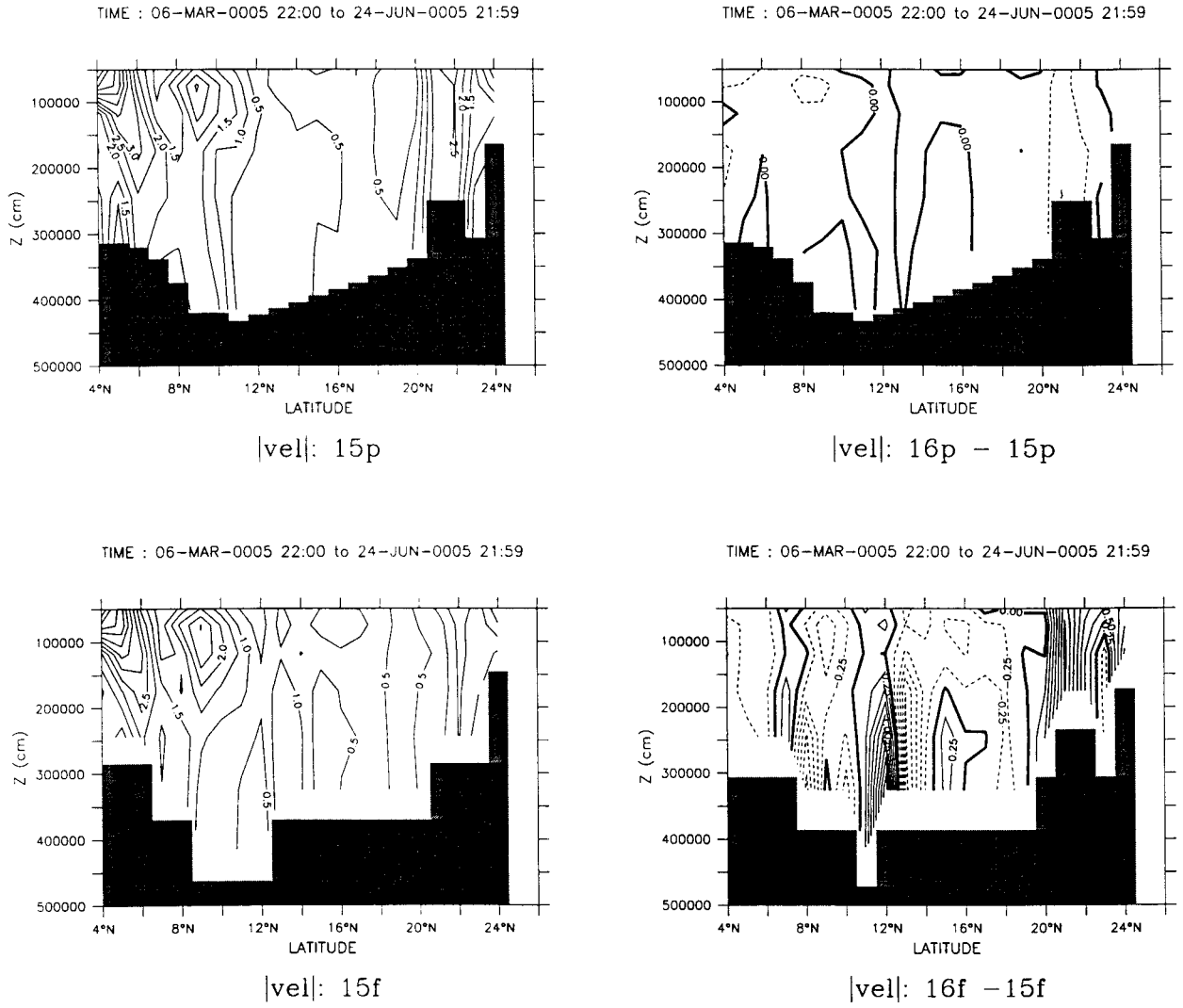

FIG. 13. Sensitivity in the amplitude of horizontal velocity along 62°E to changes in vertical levels. All results are for 3-month means from the spring of year 5. (upper left) Partial cell 15-level case. Contour interval is 0.5 cm s^{-1}. (upper right) Partial cell 16-level case minus partial cell 15-level case. Contour interval is 0.25 cm s^{-1}. (lower left) Full cell 15-level case. Contour interval is 0.5 cm s^{-1}. (lower right) Full-cell 16-level case minus full-cell 15-level case. The topography is for case 16f. Contour interval is 0.25 cm s^{-1}.

domain as a function of time is given in Fig. 17. Also plotted are the rms of the difference between cases 16f and 15f along with the rms of the difference between cases 15f and 15p. Consistent with previous results, the rms of the full cell differences is about three times larger than between partial cell cases. It is interesting to note the large difference between full cell cases during the first six months of the simulation, which is absent in the partial cell cases. Initially, there are large waves induced by the steps in the full cell discretized topography, which are eroded by friction.

The suite of four simulations 15f, 15p, 16f, and 16p were repeated using the same mixing parameterization but with twice the horizontal resolution (½°). The results of the double resolution simulations for the Arabian Sea and Bay of Bengal are given in Fig. 18. In comparison with the 1° simulations in Fig. 12, the double resolution full cell simulations have become less robust with larger differences on smaller scales, which are a result of larger topographic gradients (Δx and Δy are half as large as in the 1° case, whereas the cliffs are about the same height). Overall, the rms of the streamfunction differences are comparable to the 1° simulations. This is to be expected because the total number of ocean points scales as the square of the grid size but the number of points involved with cliffs scales with a power less than the square of the number of points.

6. Conclusions

The representation of topography significantly affects the way in which information propagates in ocean gen-

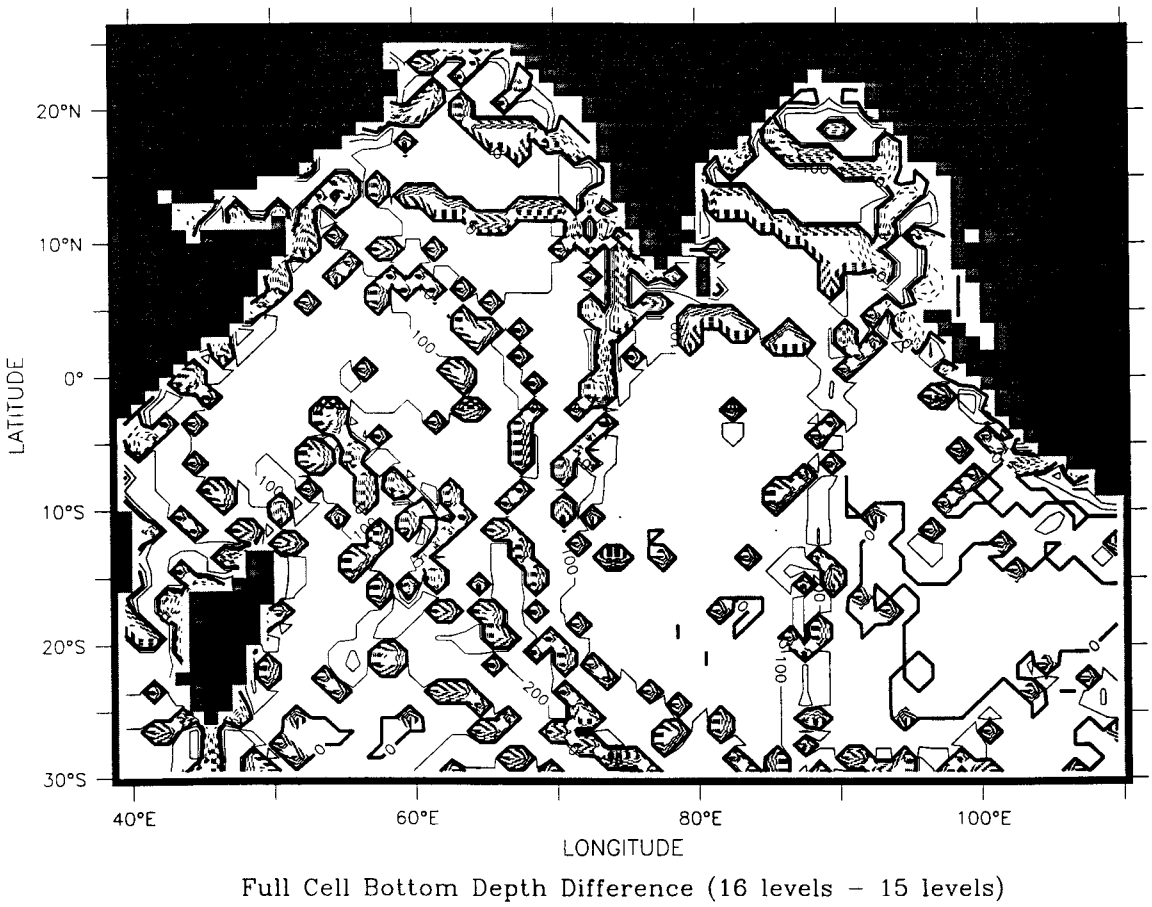

FIG. 14. Difference between discretized topography on T-cells using 15 and 16 vertical levels with full cells on a 1° horizontal resolution grid. Contour interval is 100 m. Some differences (16-level case minus 15-level case) are as follows: 81 m in the Arabian Basin (10°N, 65°E), Central Indian Basin (10°S, 80°E), and Somali Basin (0°N, 51°E): 153 m in the Bay of Bengal (8°N, 85°E) and less than 1 m in the Cocos Basin (20°S, 100°E).

eral circulation models. This paper has outlined a partial cell approach in which topography can be accurately introduced into *z*-level ocean models without introducing spurious flows due to pressure gradient errors or spurious diapycnal diffusion. The results have implications for determining energy propagation in oceanic general circulation models at both coarse and fine horizontal resolution.

The partial cell method has been added as an option to the GFDL MOM 2, which allows the model to accurately simulate topographic waves without requiring unduly high resolution in the vertical. For the cases described in this paper, the computational overhead for employing partial cells was about 10% greater than the time required for full cell simulations. For the full cell simulation to achieve the same accuracy as the partial cell simulation in resolving topographic slopes, significantly more levels would be required. This makes using full cells far less computationally efficient than using partial cells. However, coarse vertical resolution with partial cells does not achieve the same accuracy as high vertical resolution using full cells in all respects. For instance, high vertical resolution in the interior may resolve internal processes that would be missed by coarse vertical resolution and partial cells.

Within partial cells, the horizontal pressure gradient must be discretized carefully. Otherwise, pressure gradient errors can lead to nonnegligible flows. Fortunately, the bulk of the error can be removed by assuming a linear dependence of pressure with depth. The remaining error, which is typically much smaller, is due to nonlinearities in the equation of state. It should be noted that in the level above a partial cell there is a zero pressure-gradient error. Pressure gradient errors can exist only where levels intersect bottom topography. Compared to GFDL MOM 2, a true sigma coordinate model will have pressure gradient errors in all levels above the bottom. Lateral diffusion can also lead to erroneous flow with partial cells. This error can be significantly reduced by using a vertical interpolation within lateral derivatives to guarantee that no motion is induced within a linearly stratified fluid at rest.

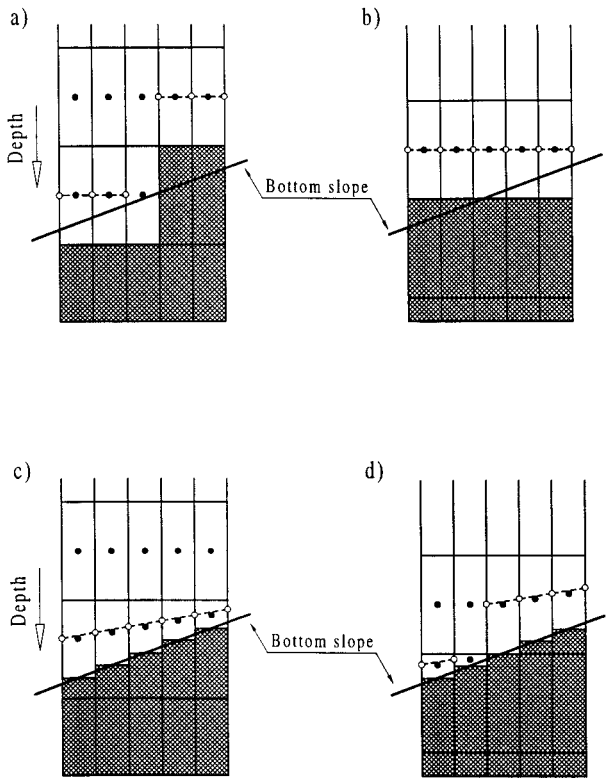

FIG. 15. Sensitivity in discretizing a sloping bottom to changes in positioning of vertical levels. (a) Using full cells. (b) Using full cells with a different arrangement of vertical levels. (c) Same as in (a) but with partial cells. (d) Same as in (b) but with partial cells.

In coarse vertical resolution ocean models, the discretization of topography makes a significant difference in how information propagates. Full cell models with poorly resolved topography propagate information according to an inaccurate dispersion relation with small-scale, relatively fast Kelvin wave–like modes, which are bottom trapped and closely follow artificial topographic ridges created by vertical discretization of the topography. By contrast, models with partial cells resolve topography better and approximate the correct dispersion relationship thereby allowing for slower, larger scale, less vertically trapped topographic waves to transmit information.

Apart from having an inaccurate dispersion relation, simulations using full cells are less robust than those using partial cells. This is because the depth of the ocean bottom is convergent (independent of the vertical coordinate) with partial cells but not with full cells. Although the depth of grid points within partial cells are not convergent, the rms differences in simulations with perturbations in the vertical coordinate are about three times larger in full cells than in partial cells. Locally, full cell simulations can be less robust than partial cell simulations by more than a factor of three.

With increasing horizontal resolution, full cell simulations continue to be less robust to perturbations in the vertical coordinate than their partial cell counterparts. The maximum differences grow as horizontal resolution is increased in full cell simulations because artificial topographic gradients increase. This is not true for partial cell solutions. However, the robustness of partial cell simulations may locally degrade to the level of full cell simulations, where changes in topography are accounted for by changes in the number of levels rather than by changes in partial cell thickness within a given level.

Although the equations drop from second order in the interior to first order for nonfull cells at the bottom, a leading-order error in the position of the topography has been corrected. Globally, the solution remains second-order accurate. It is concluded that, to a much greater extent, partial cells are relatively insensitive to vertical grid spacing, whereas full cells are not.

In one sense, it is surprising that differences between full cell and partial cell simulations are as large as they are given that the Rossby radius is largest near the equator; topography should have little influence. For this reason, it is anticipated that differences will be larger at high latitudes where the ratio of Rossby radius to topographic scales is smaller. Also, in combination with a bottom boundary layer, partial cells may alter the course taken by bottom water as it flows off shelves and along the bottom of the abyss. This may be of particular importance in regions that have gentle slope.

Acknowledgments. We wish to thank Robert Hallberg for many stimulating discussions on the importance of topographic waves. Also, we wish to thank Steve Hankin for developing Ferret[4] (Hankin 1996). All model results were produced by enabling options to save data directly in NetCDF[5] format from GFDL MOM 2 and plotting of results was done with Ferret. This combination of NetCDF and Ferret has greatly speeded up analysis of model results. There is a distortion of contour lines within partial cells because the version of Ferret that was used treats all data as if it exists at the level of the grid point within full cells. However, the next version of Ferret will accommodate sigma coordinates and therefore partial cells as well.

APPENDIX

Energy Conservation

The arguments given by Bryan (1969) for conservation of second moments (in the advection terms) rely on integrating over cell faces. Therefore, they are valid

[4] A very useful analysis package for gridded data that can accommodate the B-grid discretization of GFDL MOM 2. URL: http://www.pmel.noaa.gov/ferret/home.html.

[5] A standard method for producing self-documenting data. Information is available from URL http://www.unidata.ucar.edu.

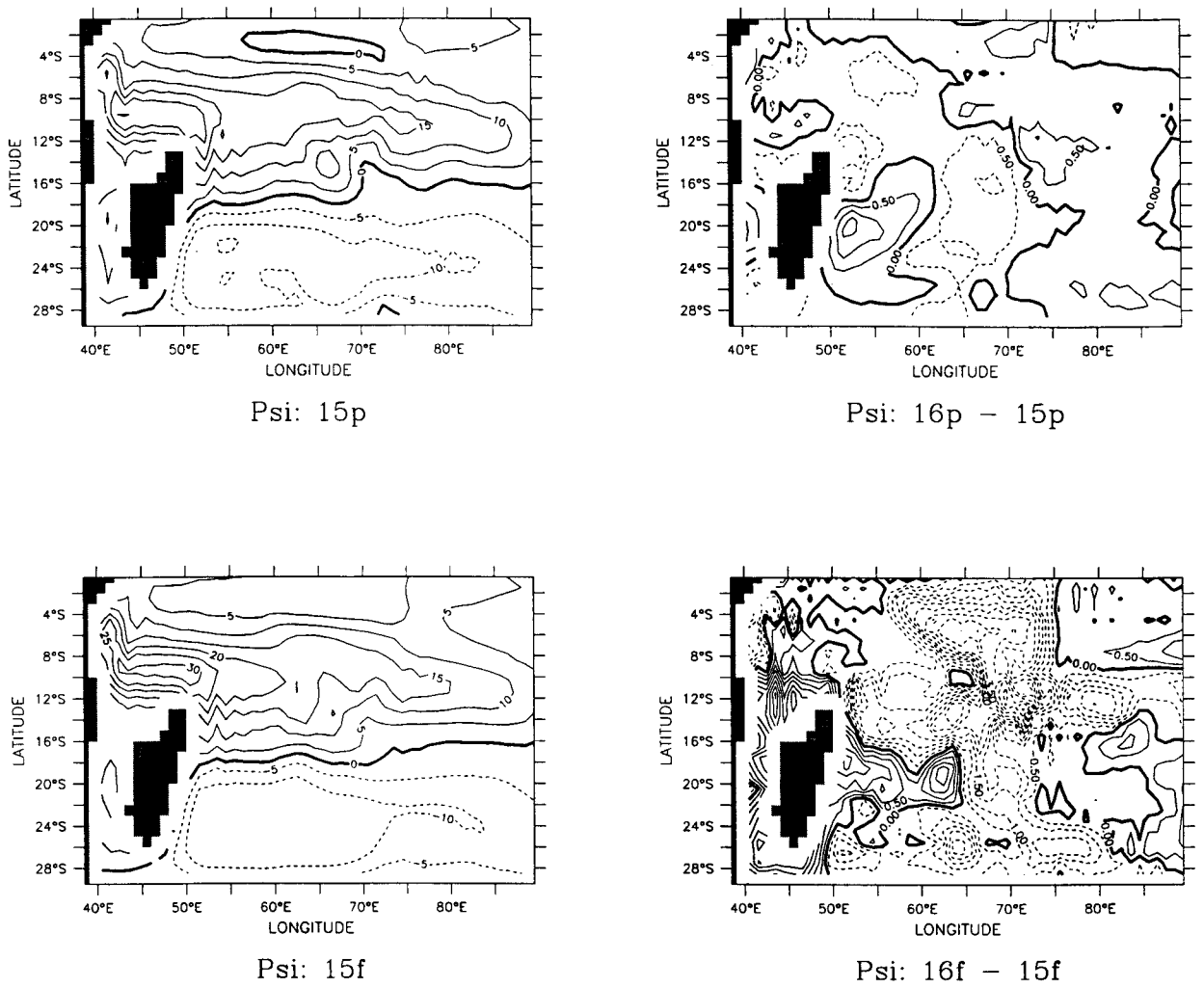

FIG. 16. Sensitivity in the horizontal streamfunction to changes in vertical levels in the Central and Southern Indian Ocean. All results are for 3-month means from the spring of year 5. (upper left) Partial cell 15-level case. Contour interval is 5.0 Sv. (upper right) Partial cell 16-level case minus partial cell 15-level case. Contour interval is 0.5 Sv. (lower left) Full cell 15-level case. Contour interval is 5.0 Sv. (lower right) Full cell 16-level case minus full cell 15-level case. Contour interval is 0.5 Sv.

for partial cells and will not be repeated here. What will be demonstrated is that a change in kinetic energy due to horizontal pressure forces is exactly balanced by a change in potential energy when density is a linear function of temperature and salinity.

Let the ocean be divided into a three-dimensional array of volume elements, which are referenced in longitude, depth, and latitude by indices *i, k, j.* Assume all variables are indexed by *i, k, j* unless otherwise noted. On an Arakawa staggered B-grid, U-cells are arranged such that the grid point within a U-cell with index *i, j* is at the northeast corner of a T-cell with index *i, j.* Zonal velocity u and meridional velocity v are defined within U-cells. Pressure P and density ρ are defined within T-cells. Refer to Fig. 4 for an illustration of the grid points and indexing.

The change in kinetic energy (KE) due to pressure forces ΔKE is given by $u\delta_\lambda(\overline{p}^\phi)$ and $v\delta_\phi(\overline{p}^\lambda)$ summed over all volume elements. This can be expressed as two summations: the first summation "ΔKE_1" accounts for pressure changes when all points within a given level are at the same depth; the second summation "ΔKE_2" accounts for the variation of grid points with depth within the same level:

$$\Delta KE = \Delta KE_1 + \Delta KE_2 \tag{45}$$

$$\Delta KE_1 = -\frac{1}{\rho_0}\sum_{i,k,j}\left[u\,\frac{1}{\cos\phi^U}\delta_\lambda(\overline{p}^\phi) + v\delta_\phi(\overline{p}^\lambda)\right] \times \Delta x^U \cos\phi^U \Delta y^U \Delta h^U \tag{46}$$

$$\Delta KE_2 = +\frac{g}{\rho_0}\sum_{i,k,j}\left[u\,\frac{1}{\cos\phi^U}\overline{\overline{\rho}^\lambda\delta_\lambda(zt)}^\phi + v\overline{\overline{\rho}^\phi\delta_\phi(zt)}^\lambda\right] \times \Delta x^U \cos\phi^U \Delta y^U \Delta h^U, \tag{47}$$

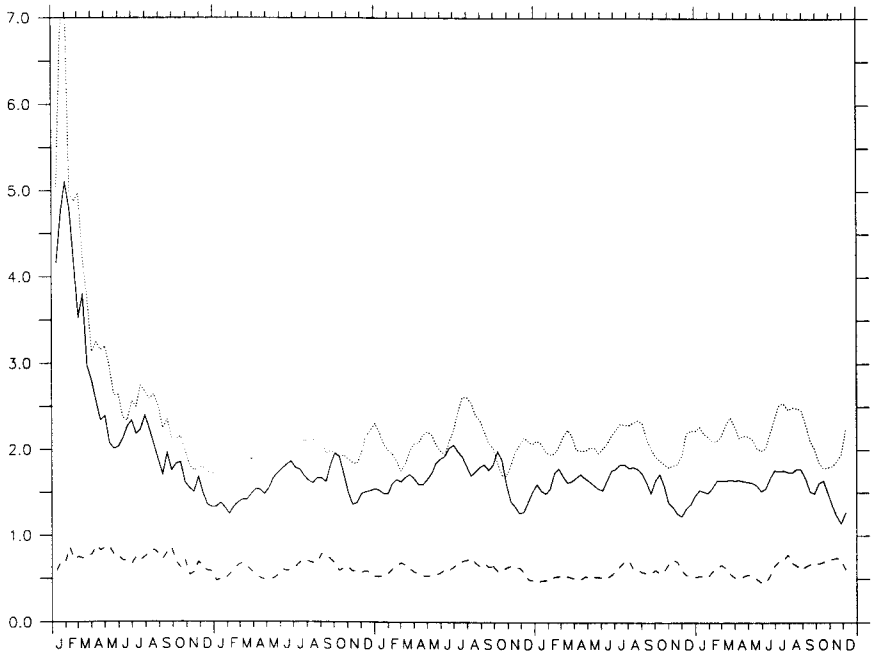

FIG. 17. Root-mean-squared value of the difference in streamfunctions between various cases taken over the entire domain as a function of time. Case 16p, case 15p (dashed line). Case 16f minus case 15f (solid line). Case 15f minus case 15p (dotted line).

where the depth of grid points *zt* is also indexed by *i, k, j*. Since velocity is zero on all boundaries, the derivative and averaging operators can be rearranged within the summations. Rearranging the derivatives within ΔKE_1 yields

$$\Delta KE_1 = \frac{1}{\rho_0} \sum_{i,k,j} [\delta_\lambda(u_{i-1})\overline{p}^{\phi} + \delta_\phi(v_{j-1}\cos\phi^{U}_{j-1})\overline{p}^{\lambda}] \times \Delta x^{U}\Delta y^{U}\Delta h^{U}. \quad (48)$$

Rearranging the averages leads to

$$\Delta KE_1 = \frac{1}{\rho_0} \sum_{i,k,j} [\overline{\delta_\lambda(u_{i-1,j-1})\Delta y^{U}_{j-1}}^{\phi}\Delta x^{T} + \overline{\delta_\phi(v_{i-1,j-1})\cos\phi^{U}_{j-1}\Delta x^{U}_{i-1}}^{\lambda}\Delta y^{T}]p\Delta h^{U}. \quad (49)$$

Note that if horizontal advective velocities on the eastern and northern face of a T-cell are defined as

$$U = \overline{u_{j-1}\Delta y^{U}_{j-1}\Delta h^{U}_{j-1}}^{\phi}/\Delta y^{T} \quad (50)$$

$$V = \overline{v_{i-1}\Delta x^{U}_{i-1}\Delta h^{U}_{i-1}}^{\lambda}\cos\phi^{U}/\Delta x^{T}, \quad (51)$$

then the summation can be rewritten as

$$\Delta KE_1 = \frac{1}{\rho_0} \sum_{i,k,j} [\delta_\lambda(U_{i-1}) + \delta_\phi(V_{j-1})]p\Delta x^{T}\Delta y^{T}\Delta h^{U}. \quad (52)$$

Continuity for each cell is expressed as

$$\frac{1}{\cos\phi^{T}}(\delta_\lambda(U_{i-1}) + \delta_\phi(V_{j-1})) + W_{k-1} - W = 0, \quad (53)$$

which further simplifies ΔKE_1 to

$$\Delta KE_1 = -\frac{1}{\rho_0} \sum_{i,k,j} p\delta_z(W_{k-1})\Delta y^{T}\Delta x^{T}\Delta h^{U}. \quad (54)$$

Rearranging the derivative yields

$$\Delta KE_1 = \frac{1}{\rho_0} \sum_{i,k,j} W_{k-1}\delta_z(p_{k-1})\Delta y^{T}\Delta x^{T}\Delta h^{W}_{k-1}, \quad (55)$$

where Δh^{W}_{k-1} is the distance between a grid point at level k and $k-1$ as indicated in Fig. 4. Using the hydrostatic equation $\delta_z(p_k) = g\,\overline{\rho_k}^{z}$ reduces ΔKE_1 to

$$\Delta KE_1 = -\frac{g}{\rho_0} \sum_{i,k,j} W_{k-1}\overline{\rho_{k-1}}^{z}\Delta y^{T}\Delta x^{T}\Delta h^{W}_{k-1}. \quad (56)$$

The second summation ΔKE_2 accounts for the variation in depth of grid points within the same vertical level. The first term in ΔKE_2 can be written as

$$\Delta KE_{2a} = -\frac{g}{\rho_0} \sum_{i,k,j} u\overline{\rho}^{\lambda}\overline{\delta_\lambda(zt)}^{\phi}\Delta x^{U}\Delta y^{U}\Delta h^{U}. \quad (57)$$

Rearranging the averaging yields

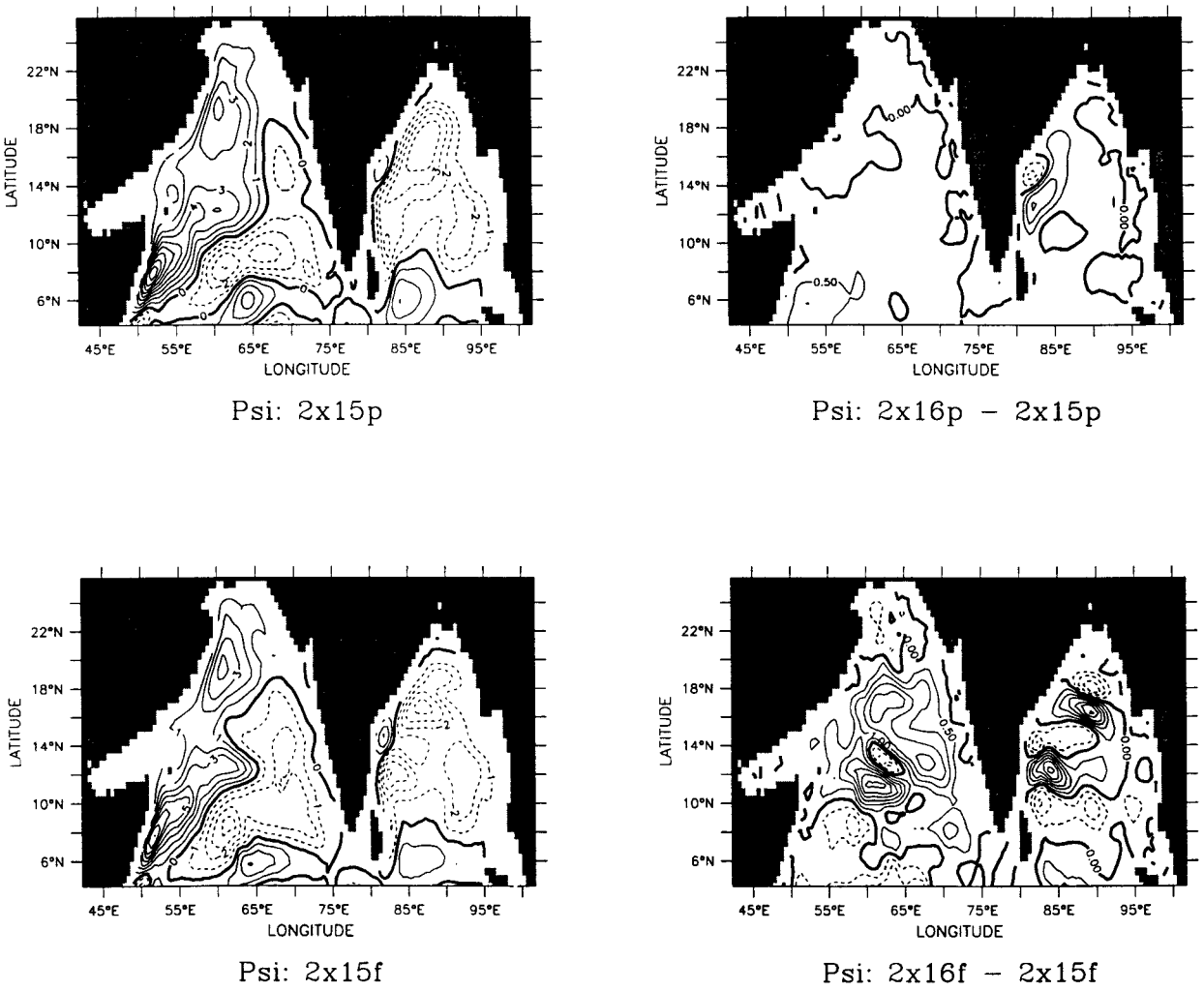

FIG. 18. Sensitivity in the horizontal streamfunction to changes in vertical levels in the northern part of the Indian Ocean with ½° horizontal resolution. All results are for 3-month means from the spring of year five. (upper left) Partial cell 15-level case. Contour interval is 1.0 Sv. (upper right) Partial cell 16-level case minus partial cell 15-level case. Contour interval is 0.5 Sv. (lower left) Full cell 15-level case. Contour interval is 1.0 Sv. (lower right) Full cell 16-level case minus full cell 15-level case. Contour interval is 0.5 Sv.

$$\Delta \mathrm{KE}_{2a} = -\frac{g}{\rho_0} \sum_{i,k,j} \overline{u_{j-1} \Delta h^{\mathrm{U}}_{j-1} \Delta y^{\mathrm{U}}_{j-1}}^{\phi} \overline{\rho}^{\lambda} \delta_{\lambda}(zt) \Delta x^{\mathrm{U}}, \quad (58)$$

which with the aid of Eq. (50) can be rewritten as

$$\Delta \mathrm{KE}_{2a} = -\frac{g}{\rho_0} \sum_{i,k,j} U \overline{\rho}^{\lambda} \delta_{\lambda}(zt) \Delta x^{\mathrm{U}} \Delta y^{\mathrm{T}}, \quad (59)$$

for which rearranging the derivative yields

$$\Delta \mathrm{KE}_{2a} = \frac{g}{\rho_0} \sum_{i,k,j} \delta_{\lambda}(U_{i-1} \overline{\rho_{i-1}}^{\lambda}) zt \Delta x^{\mathrm{T}} \Delta y^{\mathrm{T}}. \quad (60)$$

A similar manipulation reduces the second term in $\Delta \mathrm{KE}_2$ to

$$\Delta \mathrm{KE}_{2b} = \frac{g}{\rho_0} \sum_{i,k,j} \delta_{\phi}(V_{j-1} \overline{\rho_{j-1}}^{\phi}) zt \Delta x^{\mathrm{T}} \Delta y^{\mathrm{T}}. \quad (61)$$

Combining $\Delta \mathrm{KE}_1$, $\Delta \mathrm{KE}_{2a}$, and $\Delta \mathrm{KE}_{2b}$, gives the result that the change in kinetic energy due to pressure gradients is

$$\Delta \mathrm{KE} = \frac{g}{\rho_0} \sum_{i,k,j} (\delta_{\lambda}(U_{i-1} \overline{\rho_{i-1}}^{\lambda}) + \delta_{\phi}(V_{j-1} \overline{\rho_{j-1}}^{\phi})) zt \Delta x^{\mathrm{T}} \Delta y^{\mathrm{T}} - W_{k-1} \overline{\rho_{k-1}}^{z} \Delta x^{\mathrm{T}} \cos\phi^{\mathrm{T}} \Delta y^{\mathrm{T}} \Delta h^{W}_{k-1}. \quad (62)$$

If density is linear in temperature and salinity, then an equation may be written for the time rate of change of density,

$$\delta_t(\rho) = -\mathrm{Adv}(\rho). \quad (63)$$

The change in potential energy ''ΔPE'' is given as

$$\Delta \mathrm{PE} = \Delta \mathrm{PE}_1 + \Delta \mathrm{PE}_2$$

$$= -\sum_{i,k,j} zt\,\mathrm{Adv}(\rho)\Delta x^{\mathrm{T}} \cos\phi^{\mathrm{T}}\Delta y^{\mathrm{T}}\Delta h^{\mathrm{T}} \quad (64)$$

$$-\sum_{i,k,j} zt\left(\frac{1}{\Delta h^{\mathrm{T}}\cos\phi^{\mathrm{T}}}(\delta_\lambda(U_{i-1}\overline{\rho_{i-1}}^{\lambda}) + \delta_\phi(V_{j-1}\overline{\rho_{j-1}}^{\phi})) + \delta_z(W_{k-1}\overline{\rho_{k-1}}^{z})\right)\Delta x^{\mathrm{T}}\cos\phi^{\mathrm{T}}\Delta y^{\mathrm{T}}\Delta h^{\mathrm{T}}. \quad (65)$$

The change in potential energy due to the horizontal advection of density is

$$\Delta \mathrm{PE}_2 = -\sum_{i,k,j} zt(\delta_\lambda(U_{i-1}\overline{\rho_{i-1}}^{\lambda}) + \delta_\phi(V_{j-1}\overline{\rho_{j-1}}^{\phi}))\Delta x^{\mathrm{T}}\Delta y^{\mathrm{T}}, \quad (66)$$

which is the negative of $\Delta \mathrm{KE}_2$ and the vertical piece from Eq. (65) can be rearranged to

$$\Delta \mathrm{PE}_1 = \sum_{i,k,j} W_{k-1}\overline{\rho_{k-1}}^{z}\Delta h^{W}_{k-1}\Delta x^{\mathrm{T}}\cos\phi^{\mathrm{T}}\Delta y^{\mathrm{T}}, \quad (67)$$

which is the negative of $\Delta \mathrm{KE}_1$.

REFERENCES

Adcroft, A., C. Hill, and J. Marshall, 1997: Representation of topography by shaved cells in a height coordinate ocean model. *Mon. Wea. Rev.*, **125,** 2293–2315.

Baringer, M. O. N., and J. F. Price, 1997: Momentum and energy balance of the Mediterranean outflow. *J. Phys. Oceanogr.*, **27,** 1678–1692.

Beckmann, A., and R. Doescher, 1997: A method for improved representation of dense water spreading over topography in a geopotential coordinate model. *J. Phys. Oceanogr.*, **27,** 581–591.

Bleck, R., and L. T. Smith, 1990: A wind-driven isopycnic coordinate model of the North and Equatorial Atlantic Ocean. *J. Geophys. Res.*, **95,** 3273–3285.

Blumberg, A., and G. L. Mellor, 1987: A description of a three-dimensional coastal ocean circulation model. *Three-Dimensional Coastal Ocean Models*, N. Heaps, Ed., Vol. 4, Amer. Geophys. Union.

Bryan, K., 1969: A numerical method for the study of the circulation of the World Ocean. *J. Comput. Phys.*, **4,** 347–376.

——, and M. D. Cox, 1972: An approximate equation of state for numerical models of the ocean circulation. *J. Phys. Oceanogr.*, **2,** 510–514.

ETOPO5, 1988: Digital relief of the surface of the earth. Worldwide Bathymetry/Topography Data Announcement 88-MGG-02. [Available from National Geophysical Data Center, NOAA Code E/GC3, Boulder, CO 80303-3328.]

Gerdes, R., 1993: A primitive equation ocean general circulation model using a general vertical coordinate transformation. Part 1: Description and testing of the model. *J. Geophys. Res.*, **98,** 14 683–14 701.

Haidvogel, D. B., J. L. Wilkin, and R. E. Young, 1991: A semi-spectral primitive equation ocean circulation model using vertical sigma and orthogonal curvilinear horizontal coordinates. *J. Comput. Phys.*, **94,** 151–185.

Hallberg, R., 1995: Some aspects of the circulation in ocean basins with isopycnals intersecting the sloping boundaries. Ph.D. dissertation, University of Washington, 242 pp. [Available from University Microfilms, 1490 Eisenhower Place, P.O. Box 975, Ann Arbor, MI 48106.]

Hankin, S., and M. Denham, 1996: FERRET: An analysis tool for gridded data, users guide, version 4.4. NOAA/PMEL/TMAP, 243 pp. [Available from PMEL, 7600 Sand Point Way NE, Bldg. 3, BIN C15700, Seattle, WA 98115-0070.]

Hellerman, S., and M. Rosenstein, 1983: Normal monthly stress over the World Ocean with error estimates. *J. Phys. Oceanogr.*, **13,** 1093–1104.

Killworth, P. D., and N. R. Edwards, 1998: A turbulent bottom boundary layer code for use in numerical ocean models. *J. Phys. Oceanogr.*, in press.

Levitus, S., 1982: *Climatological Atlas of the World Ocean.* NOAA Prof. Pap. 13, 173 pp. [Available from U. S. Government Printing Office, Washington, DC 20402.]

Pacanowski, R. C., 1996: MOM 2 Documentation, user's guide and reference manual. GFDL Ocean Tech. Rep. 3.1, 329 pp. [Available from Geophysical Fluid Dynamics Laboratory/NOAA, Princeton, NJ 08540.]

Rhines, P. B., 1970: Edge-, bottom-, and Rossby waves in a rotating stratified fluid. *Geophys. Fluid Dyn.*, **1,** 273–302.

Semtner, A. J., 1974: An oceanic general circulation model with bottom topography. Numerical simulation of weather and climate. Tech. Rep. 9, UCLA Department of Meteorology, 99 pp. [Available from UCLA, 405 Hilgard Ave., Los Angeles, CA 90024-1565.]

Treguier, A. M., J. K. Dukowicz, and K. Bryan, 1996: Properties of nonuniform grids used in ocean general circulation models. *J. Geophys. Res.*, **101** (C9), 20 877–20 881.

Winton, M., R. Hallberg, and A. Gnanadesikan, 1998. Simulation of density-driven frictional downslope flow in *Z*-coordinate ocean models. *J. Phys. Oceanogr.*, **28,** 2163–2174.